

1 Shape of plutons in crustal shear zones: A tectono-magmatic guide based 2 on analogue models

3
4 Maria Michail ^a, Michael Rudolf ^b, Matthias Rosenau ^b, Alberto Riva ^{a,c}, Piero Gianolla ^a, Massimo Coltorti ^{a,d}

5 ^a University of Ferrara, Department of Physics and Earth Sciences, Via Saragat 1, 44122 Ferrara, Italy

6 ^b GFZ German Research Centre for Geosciences, Lithosphere Dynamics, Telegrafenberg, 14473 Potsdam,
7 Germany

8 ^c GEPlan Consulting s.r.l., Via Ariosto 58, 44121, Ferrara, Italy

9 ^d Istituto Nazionale Geofisica e Vulcanologia, Sez. Palermo, Via Ugo la Malfa 153, 90125 Palermo

10
11 Corresponding author: Maria Michail, email address: mchmra@unife.it

12 Abstract

13 Plutons in crustal shear zones may exploit and interfere with inherited structures (i.e. are post-tectonic),
14 enhance strain localizing (syn-tectonically) or deform passively (if pre-tectonic). To constrain the relative
15 timing of such tectono-magmatic constellations in natural settings is not always straight-forward. We here
16 present sandbox-type analogue model experiments simulating magma emplacement into upper crustal
17 simple and transtensional shear zones to test the diagnostic potential of pluton shape with respect to timing.
18 Observations based on fault evolution and geometrical features of the intrusions exemplify the interplay
19 between evolving and inherited tectonic structures and magma uprising. We observe markedly asymmetric
20 intrusions reflecting the regional stresses and finite strain field. At the same time, the presence of an intrusion
21 modifies the evolution of the upper crustal fault pattern, but only transiently. Diagnostic attributes include the
22 pluton's aspect ratio (length/width), its long axis orientation, amplitude and the association with dike
23 formation. Syn-tectonic intrusion models show the highest pluton amplitude among all scenarios, developing
24 lateral dikes and long-axis subparallel to the maximum horizontal stress consistent with an Andersonian
25 diking mechanism. Similarly, post-tectonic intrusion models are oriented subparallel to the inherited mode 1
26 fracture direction are exploited by roof dikes but show only a moderate amplitude and low aspect ratio. Roof
27 diking, low amplitudes and high aspect ratios, with the long-axis parallel to the finite extension direction,
28 characterizes passively sheared and rotated pre-tectonic intrusion models. Experimental results are tested
29 against observations from natural examples validating the diagnostic potential of pluton shape for the timing
30 and the tectonic setting of the emplacement.

31 1 Introduction

32 The spatial association of plutons and shear zones has long been recognized. Revealing their temporal and
33 spatial relation as a key to understand the mechanisms of tectono-magmatic interaction, is a matter of
34 research since. The interactions of tectonic and magmatic processes are often ambiguous and hard to

35 interpret (Paterson and Schmidt, 1999; Paterson and Tobisch, 1992). It is generally recognised that both
36 inherited structures and active faults represent key features in crustal-scale magma transport and
37 emplacement (Hutton 1988; Hutton and Reavy 1992; Vigneresse 1995; Román-Berdiel et al., 1997; Petford
38 et al. 2000; Handy et al., 2001; Rosenberg 2004; Corti et al. 2005; Galland et al., 2006; Galland et al. 2007b).
39 Likewise, the presence of magma in actively deforming crust may control fault localization and structural
40 evolution (e.g. Holohan et al., 2008; Dooley and Schreurs, 2012; Gomes et al., 2019). The delineated
41 scenarios of pre-, syn- and post-tectonic magmatism and the mechanisms involved remain poorly understood
42 taking also into account that gathering information from the field could be rather challenging. Beside the
43 limited outcrops in some areas, observations are, in most cases, restricted to and overprinted during the final
44 stage of magma emplacement. In addition, the deformed upper crustal layers that once hosted the magmatic
45 chamber are in most cases subject to erosion and therefore missing from the field. Consequently, the
46 information on the incremental and finite deformation has to be inferred with much effort from structural
47 indicators and the processes taking place at depth must be extrapolated (Vigneresse, 1995).

48 Modelling can help in overcoming some of the restrictions of field analysis and guide researchers by
49 identifying key observables and testing hypothesis. While all kinds of modelling have tackled tectono-
50 magmatic interaction, including analytical (e.g. Mandal and Chakraborty, 1990) and numerical modelling (e.g.
51 Burov et al., 2003), analogue models were used in particular for the typically cross-scale and four-
52 dimensional problems posed by tectono-magmatic processes (see e.g. review by Galland et al., 2015).
53 Amongst them, studies on syn-tectonic magma emplacement prevail: a) in compressional settings (Galland
54 et al., 2003, 2006, 2007; Mazzarini et al., 2010; Montanari et al., 2010); b) in strike-slip settings (Román-
55 Berdiel et al., 1997; Corti et al., 2005; Mazzarini et al., 2010; Gomes et al., 2019); c) in transpressional settings
56 (Benn et al., 1998); d) in transtensional settings (Román-Berdiel et al., 2000; Corti et al., 2003) and finally e)
57 in extensional settings (Román-Berdiel et al., 1999; Mazzarini et al., 2010; Corti et al., 2003).

58 With a few exceptions (Holohan et al., 2008; Dooley and Schreurs, 2012; Gomes et al., 2019), previous works
59 were focused on syn-tectonic intrusion scenarios. However, little evidence exists from analogue modelling
60 regarding crustal shearing of pre-tectonic intrusion scenarios. Similarly, the post-tectonic intrusion system is
61 very poorly studied, where exploitation of inherited structures from the uprising intrusion is still under debate.
62 In this paper, we aim at closing this knowledge gap and test the diagnostic potential of pluton shape for
63 relative timing with a new set of analogue model experiments simulating magma emplacement within the
64 upper brittle crust rising from a basal ductile shear zone. We conduct a systematic series of magma
65 emplacement scenarios in simple shear and transtensional regime (Fig. 1). To cover the full range of relative
66 timing, we realize pre-tectonic, syn-tectonic and post-tectonic intrusion scenarios ([Table 1](#)~~Table 4~~).

67 In contrast to earlier analogue modelling studies with a similar goal (e.g. Román-Berdiel et al., 1997; Corti et
68 al., 2005; Holohan et al., 2008; Mazzarini et al., 2010), we do not use a Riedel-type experiment with a linear
69 velocity discontinuity at the base but a more realistic distributed basal shear zone (e.g. Dooley and Schreurs,
70 2012, and references therein). The viscous-weak body, in contrast to previous work (Holohan et al., 2008;
71 Dooley and Schreurs, 2012; Gomes et al., 2019) is not lying parallel to the shear zone, but it is introduced

72 vertically and in direct contact to the shear zone. In addition, in previous work the tectonic deformation of the
73 magmatic chamber and the brittle crust, induced by the vertical upraising of the viscous body, prior to and
74 following the tectonic deformation, is not recorded. In the present study, the magmatic chamber is not
75 represented as an igneous pocket, but it is injected vertically, deforming the sand layers (no topography has
76 been added in this study) before, during and after the tectonic deformation. In addition, the weak body
77 appears with a fixed radius = 2cm, since the focus of the study is on the progressive interference with the
78 brittle crust, for all emplacement scenarios. For this reason and in contrast to previous studies (Dooley and
79 Schreurs, 2012; Zwaan and Schreurs, 2017) the intrusion geometry and the preferential orientation (angular
80 position) relative to the shear zone are not evaluated.

81 Using state of the art kinematic monitoring techniques (Digital Image correlation – DIC; Structure-from-Motion
82 – SfM), the full 3D surface deformation over time (i.e. 4D deformation) and the final intrusion three-
83 dimensional shapes are captured digitally at high resolution and accuracy. Based on this experimental data
84 set, which is openly available (Michail et al., 2020), we verify existing diagnostic features (e.g. pluton aspect
85 ratio, orientation) and new attributes (pluton amplitude, dike association) of pluton shape and validate them
86 against selected field examples. The presented models may serve as a guide to the interpretation of
87 necessarily incomplete and limited field observations.

Commentato [PP1]: Not in biblio

88 2 Methods and materials

89 2.1 Experimental setup

90 The experimental setup consists of two mobile plastic plates on a 1 by 1 m wide solid steel support platform.
91 The mobile plates are moved by linear actuators, controlled by stepper motors, in opposite direction (Fig. 1).
92 A 40-mm wide gap between the two 700 mm long and 7 mm thick mobile plates is filled with viscous material
93 (silicone oil) to allow the formation of a distributed basal shear zone, similar to natural lower crustal shear
94 zones (Fig. 1a-b). Two kinematically distinct experimental series, representing two different tectonic regimes,
95 namely simple shear (reference model RS and models of group A; Fig. 1c,e) and transtension (reference
96 model RT and models of group B; Fig. 1d,f) are presented (Table 1).

Commentato [PP2]: Questa lunghezza a cosa si riferisce?
Non abbiamo detto che sono lunghe un metro le due piastre?

97 For the simple shear regime, the gap between the mobile plates is oriented parallel to the plates' motion (Fig.
98 1c,e), while in the transtensional configuration, they are oriented with an angle, α , of 15° (Fig. 1d). Relative
99 plate velocity is fixed to 1 mm/min, for all experiments, which corresponds to a simple shear rate of $4.2 \cdot 10^{-4}$
100 s^{-1} across the width of gap resulting in a final relative displacement of the two sides of the shear zone of 60
101 mm for all experiments. A low shear rate, together with a viscous fluid, rough inner edges of the mobile plates
102 and polished and lubricated surface of the metal base, result in a well distributed deformation within the gap
103 although minor localization of shear and extension at the shear zone boundaries is unavoidable. Simple shear
104 and transtensional models are run under dextral and sinistral senses of shear, respectively, in order to ease
105 their distinctness.

106 A 40-mm thick, sieved quartz sand layer representing the brittle upper crust (Fig. 1a-b) covers the mobile
107 plates and the basal shear zone. On top of each mobile plate, fixed, motion-parallel sidebars confine the sand
108 layer laterally and helps in model preparation (Fig. 1a,e). In the centre of the basal shear zone, a motor-
109 controlled piston pushes silicone oil up through a pipe (with 40 mm diameter) placed beneath the
110 experiment's foundation, to simulate the magma ascending from the lower crust into the upper-crustal shear
111 zone (Fig. 1e-f). (Fig. 1). The piston moves at a velocity of 1 mm/min, which translates into an injection rate
112 of 21 mm³/s for all experiments (Table 1). All the experiments are performed under air-controlled ambient
113 conditions (23°-25°C, 50% humidity).

114 2.2 Analogue materials

115 The viscous analogue material used for both the intrusion and the basal ductile layer is a silicone oil (Polydi-
116 methylsiloxane PDMS, G30M by K. Obermeier GmbH). It has a density of 965 kg m⁻³ and a Newtonian
117 viscosity of 22.4 kPa s at laboratory strain rates below 10⁻² s⁻¹ (Rudolf et al., 2016; see [Table 2](#)). Earlier
118 studies showed that similar material is a suitable analogue for ductile lower crust and, at reduced viscosity,
119 for low density-high viscosity (i.e. granitic) magmas simulation (e.g. Román-Berdiel et al., 1997; Benn et al.,
120 1998, 2000; Galland et al., 2015). We here use one material for simulating both the ductile lower crust and
121 the magma in order to reduce rheological complexity but also due to practical reasons, i.e. to avoid gravita-
122 tional flow of the material at the end of the experiment and to allow manual excavation of the ductile shear
123 zone and the intrusion.

124 Sieved dry quartz-sand (G12) functions as brittle analogue of the upper crust. The sand is a well-sorted, well-
125 rounded and fine-grained (<400 μm) sand of fluvial origin (Klinkmüller et al., 2016; Rosenau et al., 2018).
126 When sieved, a bulk density $\rho \sim 1600 \text{ kgm}^{-3}$ is reached and the sand layer is characterized by internal friction
127 coefficients μ of 0.69, 0.62, 0.55 (static, reactivated, sliding) and a cohesion C in the order of 50 - 110 Pa
128 (Table 1). The localization behaviour of sand produces shear zones several grain diameters wide rather than
129 idealized infinitely narrow faults. However, we here use the term "faults", to describe the small-scale shear
130 zones, evolving in the analogue model because of the generally close dynamic similarity (Ritter et al., 2016).
131 With the term "shear zone" in contrast we refer to the regional deformation zone composed of several faults
132 evolving on top of the basal ductile shear zone.

133 2.3 Scaling and Similarity

134 The experiments are scaled following the principles of geometric, kinematic and dynamic similarities to the
135 natural prototype (Hubbert, 1937; Ramberg, 1981; Weijermars and Schmeling, 1986). Accordingly, for a
136 brittle-viscous sandbox model under normal gravity, the stress scaling dictates the length and time scaling.
137 In the pressure-dependent brittle regime and under normal gravity, the length scale L^* can be delineated from
138 densities and cohesion in the model and prototype following the scaling law:

$$139 L^* = C^* / \rho^* \quad (i)$$

140 where the asterisks denote the model/prototype ratios known as the scaling factors (i.e. $C^* = C_{model}/C_{prototype}$).
141 Inserting numbers for the scaling factors for density and cohesion of our brittle analogue rock material (C_{model}
142 ~ 10 -100 Pa, $\rho_{model} = 1600$ kg/m³) and typical upper crustal rocks ($C_{prototype} = 10$ MPa, $\rho_{prototype} = 2600$ kg/m³)
143 yields a length scaling factor of L^* in the order of 0.6 - 6×10^{-6} , i.e. 1 cm in the model equals 0.6-6 km in nature
144 (Table 2). Consequently, our model represents an intrusion into the upper 2-20 km thick crust. For our models,
145 due to dimensional identity, the stress scale is also fixed by the choice of cohesion to $\sigma^* = 1$ - 10×10^{-6} .

146 In the strain-rate dependent viscous regime the time-scale T^* can be delineated, based on dimensional
147 arguments, from the viscosities η in the model and in nature using the formerly set stress scale and following
148 the scaling law

149 $T^* = \eta^* / \sigma^*$. (ii)

150 With the viscosity of the silicone oil ($\eta_{model} \sim 10^4$ Pas) and considering a typical viscosity range for magma
151 ($\eta_{prototype} = 10^4$ - 10^{10} Pas), this scaling yields highly unsuitable laboratory time scales, that require running the
152 experiments at even lower rates than in nature. This dilemma has already been noticed by Ramberg (1981)
153 who stated that magma cannot be properly scaled because even the most viscous (low water content, high
154 silica) magma would require an analogue fluid, which is even less viscous than water and which does not
155 exist.

156 To solve this dilemma, we here consider the rising magmatic body not as a homogenous melt with low
157 viscosity but as a succession of rapid melt injections into the crust over millions of years. This is in accordance
158 to the general view that plutons grow transiently over the Ma timescale fed by magma that transits through
159 lower crustal shear zones episodically on the hundreds to thousands of years timescale (e.g. Handy et al.,
160 2001, Patterson et al., 2011, Brown, 2013). The resulting magmatic system has therefore an effective bulk
161 viscosity much higher than that of the individual melt components and which is more similar to ductile lower
162 (quartz-feldspatic/andesitic) crust at typical regional tectonic strain rates ($\eta_{prototype} > 10^{20}$ Pas at $< 10^{-14}$ s⁻¹, e.g.
163 Shinevar et al, 2015). Such an alternative interpretation of the analogue model is not only consistent with
164 modern views of episodic pluton growth but considers at the same time, though highly simplified, thermal
165 aspects of the emplacement process (i.e. cooling and crystallization between injection episodes; Gomes et
166 al., 2019). Following this reasoning and considering a Million-year time scale of pluton growth, we derive the
167 time scale by relating the filling times of our model pluton (ca. 10^{-8} m³/s) to mean natural rates of 10^2 km³/Ma
168 (e.g. Patterson et al. 2011). Accordingly, we arrive at $T^* = 10^{-13}$ (1 second in the lab corresponds to ca. 30.000
169 years, Table 2). According to this timescale the applied velocity of 1 mm/min scales to ca. 0.5 mm/a in nature
170 and a corresponding shear rate of ca. 10^{-17} s⁻¹.

171 2.4 Monitoring and Analysis

172 We use state-of-the-art digital image correlation techniques for kinematic monitoring of the model surface
173 deformation (Particle Image Velocimetry, PIV) and for deriving the surface topography and intrusion shape
174 (Structure-from-Motion, SfM). All digital data generated in this study are published open access in Michail et
175 al. (2020).

Commentato [PP3]: Questa viscosità è decisamente troppo elevata per la nostra intrusion, a meno che non consideriamo il crystal mush durante il raffreddamento, ma non mi sembra ci siano evidenze di isorientamento dei cristalli in sezione

Commentato [PP4]: Dalle ultime datazioni sul vulcanismo i tempi sarebbero più brevi, anche se non è detto che il plutonismo abbia tempi comparabili

2.4.1 Particle Image Velocimetry (PIV)

A stereoscopic pair of charge-coupled device (CCD) cameras (11 MPx, 14bit, LaVision Imager ProX) monitor the model surface during the experimental run at a frequency of 0.3 Hz (Fig. 2a). Digital image correlation, using a least square minimization technique (as implemented in LaVision Davis 8), allows a quasi-continuous quantitative monitoring of the topographic evolution and surface deformation at high spatio-temporal resolution according to the principles of PIV (Adam et al., 2005). We derive 3D incremental and cumulative surface deformation pattern (i.e. velocity fields, strain fields and topography) at the sub-millimetre resolution.

From the surface velocity field, we produce surface strain maps which show the incremental shear strain E_{xy} (the unit of which is millistrain, mS), highlighting active faults and their kinematics. Positive values (red colors in all Figures) indicate a clockwise rotation or dextral shear sense and negative values (blue colors in all Figures) indicate anti-clockwise rotation or sinistral shear. The final shear strain is computed as the cumulative (or finite) displacement field indicating the relative importance of individual faults in accommodating deformation over the full experimental range.

2.4.2 Structure-from-Motion (SfM)

To obtain the 3D model reconstruction of the final topography (digital elevation model, DEM) and the final intrusion shape (digital intrusion model, DIM) at high resolution we rely on the Structure-from-motion (SfM) technique (Westoby et al., 2012) using digital images taken at the end of every experiment with a customer grade DSLR camera (NIKON D80, 10 MPx). Images including perspective views of both the final model surface and the model intrusion after excavation taken from various angles are used for the 3D model reconstruction achieved by using Agisoft PhotoScan (Professional Edition). For visualization coloured DIM-contours have been extracted from the models.

The intrusion's geometry (pluton shape) is quantified using various dimensionless parameters derived from the DIM:

First, its normalized amplitude

$$A_{\text{intrusion}} = H_{\text{intrusion}} / H_{\text{sand layer}} \quad (\text{iii})$$

where $H_{\text{intrusion}}$ is the intrusion height above the initial surface of the ductile layer and $H_{\text{sand layer}}$ is the thickness of the sand layer (i.e. 40 mm). Second, the aspect ratio

$$r = L/W \quad (\text{iv})$$

calculated based on the length L and width W of the ellipse that fits to the DIM perimeter at a given contour level.

Third, the orientation of the intrusion, which is described by θ , defined as the angle between the long axis L of the fitted ellipse and the strike of the basal shear zone. θ is counted counter clockwise. Aspect ratio and angle of intrusion are derived for each contour level and allows analysis of the shape as a function of height.

209 3 Experimental results

210 Nine experiments in total are presented and discussed in the following sections (Table 1-4): i) three
211 reference experiments (Group R); ii) three models of intrusion under (dextral) simple shear (Group A) and iii)
212 three models of intrusion under (sinistral) transtension (Group B). Pre-, syn and post-tectonic intrusion
213 scenarios are presented for the Groups A and B. Group R consists of a static intrusion without applied shear
214 (R0), a simple shear (RS) and a transtensional experiment (RT), both without intrusion. Rates of intrusion
215 and deformation are kept constant in all experiments as well as the thickness of the brittle layer.

216 3.1 Reference models (Group R)

217 The surface evolution of the reference experiments, namely the static intrusion model (R0; Fig. 2a-c), the
218 simple shear model (RS; Fig. 2d-f) and the transtension model (RT; Fig. 2g-i) is summarised in Fig. 2. In the
219 R0 model, a circular sand dome starts to form above the intrusion as soon as the injection has started ($V_{inj} =$
220 3.2 ml ; Fig. 2a). Gradually, the sand layer forms an elongated rectangular domal uplift preserved until the
221 latest intrusion stage, bound by lateral reverse faults, parallel to the basal ductile layer (Fig. 2b-c). The uplift
222 rate decreases with time.

223 For the reference experiments under simple shear (RS) and transtensional (RT) deformation the surface
224 evolution shows a typical sequence of structures consistent with previous studies using a distributed basal
225 shear zone and dry sand layers (Román-Berdiel et al., 1997; Corti et al., 2005; Dooley and Schreurs, 2012).

226 In the very early evolution stage of the RS model ($d_{rel} = 5.0 \text{ mm}$) a diffuse belt starts to form above the basal
227 ductile shear zone (Fig. 2d). With increasing displacement, early en-échelon synthetic Riedel shears (R)
228 develop with a trend of $\sim 20^\circ$ to the trace of the basal shear zone ($d_{rel} = 16.1 \text{ mm}$; Fig. 2e). Lower-angle
229 synthetic shears develop between the overlapping R shears, having a strike of $\sim 15^\circ$ (Fig. 2e). The final
230 deformation surface pattern ($d_{rel} = 38.3 \text{ mm}$) is characterised by the formation of an active and continuous
231 master fault (MF), as a result of the linkage of the individual early shear structures, parallel to the basal shear
232 zone, along which less active anastomosing minor faults which define shear lenses and pop-up structures
233 ($d_{rel} = 38.3 \text{ mm}$; Fig. 2f). The final surface width of the shear zone (ca. 50 mm) is larger than the basal shear
234 zone (40 mm ; Fig. 2f).

235 The transtensional reference experiment (RT) shows an early evolutionary history similar to the simple shear
236 experiment with the formation of a diffuse shear zone above the basal ductile shear zone (Fig. 2g-i). Linkage
237 of early right-stepping and overlapping R shears occur along lower angle structures (Y, P shears) causing a
238 deformation localization in the central part and forming a through-going master fault from early on ($d = 11.1$
239 mm ; Fig. 2g-h). During the final stage, the deformation partitions between lateral faults and fault-bounded
240 rhomboidal basin structures (Fig. 2i). In this stage, the pull-apart basin structure is cut short by strike-slip
241 faults that continue to propagate towards the dominating parallel boundary faults. This results in lengthening
242 and narrowing of the pull-apart basin in a direction parallel to the displacement vector. The final surface width
243 of the shear zone is larger (ca. 60 mm) than the basal shear zone (44.4 mm ; Fig. 2i).

244 3.2 Simple shear intrusion models (Group A)

245 3.2.1 Effect of intrusion on fault pattern

246 The three models presented in this group show the evolution of deformation with the presence of analogue
247 magma injection that predates (A1, pre-tectonic model), coincides (A2, syn-tectonic model) and post-dates
248 (A3 post-tectonic model) the applied simple shear deformation. Our observations focus on the interactions
249 taking place between faulting and intrusion and how they affect the fault pattern evolution and the final
250 intrusion geometry.

251 The pre-tectonic intrusion experiment, model A1 (Fig.3), consists of two parts: during the first half of the
252 experiment, static intrusion takes place ($V_{inj} = 37.3$ ml) causing a domal uplift ($\Delta h_{init} = 7$ mm, Fig. 3a) as
253 described for the R0 model (Fig. 2a-c). In the second half of the experiment, following the static intrusion,
254 dextral shearing is applied. Accordingly, in the early intrusion stage there is no obvious fault formation (Fig.
255 3a). Once shearing started diffuse deformation and Riedel shears occur in a spindle-like surface area ($d_{rel} =$
256 11.4 ; Fig. 3b) forming a wider shear domain bound by transpressional faults. At a later stage of shearing (d_{rel}
257 $= 22.2$ mm; Fig. 3c) a system of strike-slip faults consisting of two lateral and one central fault is cutting
258 through the uplifted domain. The finite fault pattern (Fig. 3d-f) is, in contrast to the model RS, characterized
259 by a wider strike-slip system encompassing the intrusion area and external transpressional faults which have
260 been active mainly during early stages of deformation.

261 The fault pattern in the syn-tectonic intrusion experiment, model A2 (Fig. 4), initially evolves in a similar
262 fashion as in model A1. In the early deformational stage ($d_{rel} = 3.9$ mm; $V_{inj} = 4.9$ ml; Fig. 4a) a diffuse spindle-
263 like shear zone occurs encompassing the uplifting centre. With ongoing shearing and intrusion ($d_{rel} = 6.7$ mm;
264 $V_{inj} = 4.9$ ml, Fig. 4b) transpressional faults localize at the periphery of the spindle-like area embracing the
265 intrusion domain as well as Riedel shear in the centre. In the late stage ($d_{rel} = 27.8$ mm; $V_{inj} = 35.0$ ml; Fig. 4c)
266 deformation localizes into a narrow strike-slip fault system cutting the intrusion area. This set of parallel,
267 locally transtensional faults cause the depressing of the uplifted central domain (Fig. 4e). The finite fault
268 pattern (Fig. 4d-f) shares characters of the reference model RS (a central strike-slip fault system; Fig. 2d-f)
269 and the pre-tectonic model A1 (early stage transpressional faults swinging around the intrusion area; Fig.
270 3b).

271 The post-tectonic experiment, model A3 (Fig. 5) consists again of two parts: In the first half, the experiment
272 follows according to the observations documented for the RS model ($d_{rel} = 30$ mm; Fig. 2d-f) resulting in a
273 system of strike-slip faults (Fig. 5a) at the start of intrusion. In the second half of the experiment, static
274 intrusion causes formation of new lateral faults (in the "south" of the intrusion) but also the reactivation of
275 inherited, lateral faults (in the "north" of the intrusion; $V_{inj} = 12.6-32.2$ ml; Fig. 5b-c). Importantly, active faults
276 in opposite corners of the intrusion show a synthetic sense including dextral and sinistral shear (Fig. 5b-c).
277 Consequently, dextral displacement across inherited faults acquired in the first half of the experiment is now
278 partly inverted. The finite fault pattern (Fig. 5d-f) is a composite of partly re-activated strike-slip faults similar
279 to the reference model R0 (Fig 2h-i) and new reverse faults embracing a central domal uplift.

3.2.2 Effect of deformation on intrusion shape

Among the three emplacement scenarios there is a significant variation regarding the final geometrical features of the intrusion described by the intrusion's absolute height (H) and normalized amplitude (A), its aspect ratio ($r = \text{length}/\text{width}$) and the orientation of its long axis (angle θ). The intrusion models appear strongly deformed and asymmetric, revealing the tectonic impact during their emplacement, and have a systematic generic relation to the regional stress and finite strain fields (Fig. 6).

The intrusion of Model A1 (pre-tectonic, Fig. 6a-d), which has been passively deformed is characterized by low height and amplitude ($H_{A1} = 15 \text{ mm}$, $A_{A1} = 0.38$), compared to intrusions from other scenarios. Its asymmetry is related to displacement along the crosscutting faults developing late in the experiment. The lower part of the intrusion represented e.g. by the contour level $c_1 = 3\text{mm}$ shows a relatively high aspect ratio ($r_1 = 2.7$) with the long axis of the intrusion forming a low angle of $\theta_1 = 12^\circ$ to the shear zone. At higher contour levels the intrusion progressively elongates ($r > 3$) and rotates (e.g. $\theta_2 = 34^\circ$ at $c_2 = 12\text{mm}$) becoming subparallel to the elongation direction of the finite strain tensor, ϵ_1 (Fig. 7). The intrusion roof is sculpted by one central and two lateral ridges that represent silicone oil intruding upwards along the master fault (MF) and the lateral faults, obviously during the post-intrusion stage of the experiment.

The intrusion Model A2 (syn-tectonic, Fig. 6e-h) is characterized by an acute roof resulting in a significant height and amplitude ($H_{A2} = 24\text{mm}$; $A_{A2} = 0.6$; Fig. 6e-f) compared to intrusions from other scenarios. It shows a strong asymmetric wing shape with opposing orientation to the intrusion model A1. At lower levels, the intrusion has a high aspect ratio (e.g. $r_1 = 2.5$ at $c_1 = 5\text{mm}$) with the long axis almost parallel to the shear zone ($\theta_1 = 1^\circ$). Upwards, the intrusion progressively rotates into the orientation of Riedel shears (e.g. $\theta = -10^\circ$ at $c_2 = 20\text{mm}$) while keeping its aspect ratio rather constant (Fig. 7). Lateral ridges flank the central upheaval with all of them exploiting faults formed during intrusion. The wing shape of the intrusion in association with scissor tailed and offset apophyses appears unique to this scenario.

The intrusion Model A3 (post-tectonic, Fig. 6i-l) is characterized by a more domal shape with intermediate height and amplitude ($H_{A3} = 22 \text{ mm}$; $A_{A3} = 0.55$). It appears sub-circular to gently elongated ($r < 2$) and largely subparallel to the shear zone with no systematic change of aspect ratio and orientation with height (Fig. 7). The roof is rounded and sculpted by a central ridge ($r_2 = 1.9$ at $c_2 = 19\text{mm}$) and two lateral ridges exploiting inherited structures (Fig. 6i-j).

3.3 Transtensional intrusion models (Group B)

3.3.1 Effect of intrusion on fault evolution

Transtensional intrusion experiments demonstrate, similarly to Group A, ongoing interactions developing between the intrusion and the fault pattern evolution for all three time-related intrusion emplacement scenarios.

In the first half of the pre-tectonic intrusion experiment, model B1, static intrusion takes place ($V_{inj} = 37.7 \text{ ml}$), deforming the initially flat topography and causing a domal surface uplift ($\Delta h > 10\text{mm}$) above the centre (Fig.

316 8a), as described for the R0 model (Fig.2a-c). In the second half of the experiment, transtension is applied
317 and a diffuse spindle-like shear zone with oblique Riedel shear to form ($d_{rel} = 5.6$ mm; Fig. 8b) similar as in
318 the pre-tectonic simple shear model A1. With ongoing transtension lateral faults and Riedels localize
319 deformation ($d_{rel} = 16.7$ mm; Fig. 8c) there is a subsidence along the shear zone. The initial central dome is
320 crosscut by a fault system (P and Y-shears) that links the northern and southern boundary faults, that remain
321 active until the completion of the experiment (Fig. 8c-f). En-echelon arrays of oblique extension form within
322 the basin (Fig. 8d). The finite deformation pattern of the surface is characterised by a well-defined elongated
323 pull-apart basin (Fig. 8d-f). The domal uplift, caused by the static intrusion, is overprinted and appears as a
324 remaining gentle uplift in the centre (Fig. 8e). Notably, the topographic expression of intrusion is much less
325 than in the corresponding simple shear model A1 (Fig. 3e).

326 The early stage of the syn-tectonic intrusion experiment, model B2, is characterized by diffuse shear and the
327 Riedel shear formation ($d_{rel} = 1.2$ mm; $V_{inj} = 1.5$ ml; Fig. 9a). At an intermediate stage ($d_{rel} = 8.3$ mm; $V_{inj} =$
328 10.5 ml) and along with subsidence the linkage of these Riedel shears form a fault zone that diverges from
329 the strike of the basement-fault system to a releasing stepover centred on the weak zone (Fig. 9b). At
330 a late stage ($d_{rel} = 16.7$; $V_{inj} = 21$; Fig. 9c) extensional faults bound the outer basin margins and curve towards
331 the centre (Fig. 9c). As the master fault continues to propagate, it crosscuts and deforms the evolving basin.
332 The finite fault pattern (Fig. 9d-e) is, in contrast to the reference model RT (Fig. 2g-i), characterised by
333 segmented or curved faults bounding the elongate basin with the deep central graben flanked by horst blocks.

334 The post-tectonic intrusion experiment, model B3 (Fig. 10), is divided in two parts: during the first half the
335 deformational style supports the observations mentioned for the RT model (Fig. 2g-i), resulting in a fault-
336 controlled, spindle-shaped pull-apart basin ($d_{rel} = 30$ mm; Fig. 10a; d). Following the first half, static intrusion
337 ($V_{inj} = 13$ ml) starts to form a domal uplift, triggering the re-activation of the pre-existing faults (Fig. 10b).
338 Similarly observed in model A3, cross-intrusion faults form in response to surface uplift, separating blocks
339 with differing shear sense; active faults in opposite corners of the intrusion show a synthetic sense including
340 dextral and sinistral shear (Fig. 10b-c). Sinistral displacement overprints the re-activated inherited master
341 fault trace, while the displacement seems partly inverted along the boundary fault system ($V_{inj} = 18.6$; Fig.
342 10c). The finite topography (Fig. 10d-e) reflects, in contrast to the reference model RT, the emplaced
343 magmatic chamber and the late surface uplift within the basin system (Fig. 10d-e).

344 3.3.2 Effect of deformation on intrusion geometry

345 The intrusion Model B1 (pre-tectonic, Fig. 11a-d) appears elongated and extends along the boundary faults.
346 Post-emplacement tectonic thinning in the transtensional regime results in additional and characteristic flat-
347 tening and lowering of the intrusion's height ($H_{B1} = 5$ mm, $A_{B1} = 0.13$). The intrusion's aspect ratio shows
348 characteristic high values with no systematic change with height (Fig. 7), varying from 1.8 at $c_1 = 1$ mm (Fig.
349 11c) to 1.9 at $c_2 = 3$ mm (Fig. 11d). The intrusion follows a steady and increasing trend with height, tending to
350 become subparallel to the finite strain tensor, ϵ_1 (Fig. 7). The principal axis, at lower contour levels forms a
351 low angle of $\theta_1 = 28^\circ$ to the sinistral transtensional shear zone and at $c_2 = 3$ mm an angle of $\theta_2 = 42^\circ$ (Fig. 12).

352 The intrusion's flat roof is overprinted by lateral ridges in the "south" and "north" flank of the intrusion, devel-
353 oped during the post-emplacement deformation.

354

355 The intrusion Model B2 (syn-tectonic; Fig. 11e-h) is characterised by a rounded-smooth roof of $H_{B2} = 22$ mm
356 ($A_{B2} = 0.6$) height. The intrusion's ellipse at the lower contour level, $c_1 = 5$ mm, shows an aspect ratio of $r_1 =$
357 1.7 with the long axis forming a low angle of $\theta_1 = -10^\circ$ (Fig. 11g), with opposing orientation to the intrusion
358 model B1. Towards higher contour levels, the intrusion's ellipse at $c_2 = 12$ mm shows similar aspect ratio and
359 a higher trend ($\theta_2 = -19^\circ$), subparallel to the maximum stress orientation, σ_1 (Fig. 11h; Fig. 12). This model
360 bears a smooth roof top and lateral ridges flanking the central upheaval. The asymmetric wing shape marked
361 by a scissor tail apophyses that trails behind the intrusion, are similarly observed for model A2 (Fig. 6e-h).

362 Finally, the intrusion Model B3 (post-tectonic, 11j-l) regards a sub-circular to slightly elongated intrusion of
363 domal shape ($H_{B3} = 20$ mm; $A_{B3} = 0.5$). At lower contour levels ($c_1 = 4$ mm), the intrusion's ellipse shows an
364 aspect ratio of $r_1 = 1.4$ with the long axis parallel to the shear zone (Fig. 11k). This model is characterised by
365 an asymmetric roof of carrying a central ridge ($r_2 = 1.7$ at $c_2 = 18$ mm,) and two lateral ridges (Fig. 11l). At
366 higher contour levels, the axis trend appears subparallel to the maximum stress orientation, σ_1 ($\theta_2 = -11^\circ$;
367 Fig. 7).

368 4 Discussion of experimental results

369 First order observations based on testing different scenarios of analogue magma intrusion by varying the
370 relative timing of magma emplacement with respect to the regional tectonic deformation along the shear
371 zone, in simple shear and transtensional deformation, are analysed and presented in this study. The intrusion
372 experiments distinguished in pre-, syn- and post-tectonic emplacement are divided in two groups: simple
373 shear (Group A) and transtension (Group B). The results offer a broader view on the relations developing
374 between magmatism and deformation, as reported similarly in previous works, plus constitute an important
375 contribution in defining key-features on the geometry of intrusions, that reveal their emplacement mode along
376 shear zones.

Commentato [PP5]: Questo in realtà è già stato detto all'inizio....

377 4.1 Model boundary conditions, simplifications and limitations

378 *Effect of the basal ductile shear zone on the emplacement process*

379 We use a ductile homogenous shear zone as a basal kinematic boundary condition, which mimics a natural
380 mid-crustal shear zone. Apart from distributing deformation, the ductile material also influences the
381 emplacement mechanisms as reported in previous studies (Román-Berdiel et al., 1997; 2000; Corti et al.,
382 2005; Montanari et al., 2010; Mazzarini et al., 2010). In those models, the presence of a widespread ductile
383 layer is a pre-requisite to allow lateral flow and emplacement in laccolith style. It is suggested that for the syn-
384 intrusive deformation the rheological stratification caused a deeper level of emplacement with respect to
385 purely brittle models and thus controls the timing of magma emplacement. For our experiments, instead of a
386 widespread ductile layer, we introduced a basal ductile band. Intrusions are allowed within the ductile band

387 and above the fixed injection tube. The effects described previously is similarly active in our setup with lateral
388 intrusion aided by the ductile material.

389 *Ignoring thermal and strain-rate dependent effects on rheology.*

390 The deformation in our experiments was accomplished by a quasi-stationary rheology including temperature-
391 and strain rate-insensitive brittle and Newtonian viscous materials. Our modelling faces therefore some
392 limitations regarding rheological principals (Corti et al., 2003). Magma cooling is considered in simplified way
393 by choosing a relatively high viscosity of the model magma (see chapter on scaling and similarity 2.3).
394 Thermal effects caused by the intrusion-related heating on the rheology of the crustal rocks were not taken
395 into consideration for our modelling as for all other models of this type (Román-Berdiel et al., 1997; Corti et
396 al., 2003; Galland et al., 2003, 2006, 2007; Montanari 2010; Mazzarini 2010). At shallow crustal levels as
397 those targeted here, intrusion of rather small amounts of hot material into cold crust has likely a minor effect
398 on the geotherm and thereby on the rheology in general. However, the brittle-ductile transition might be more
399 sensitive to even small fluctuations in the geotherm caused by episodic heat advection by veining and long-
400 term emplacement of the intrusion (e.g. Handy and Streit 1999; Brown, 2013). Any modification of the
401 rheology around the base of our models including temperature and strain-rate dependent viscosity changes
402 or even switches in the dominant deformation mechanisms (and thereby the geometry of the brittle-viscous
403 transition) is however beyond the scope of this modelling approach. While we consider this drawback of the
404 method more significant at a small scale, numerical modelling might help in verifying the validity of our
405 stationary approach on a regional scale.

406 *What drives deformation in the model versus nature?*

407 In our experiments model magma is rising due to two different forces: pressure applied externally and internal
408 buoyancy forces (e.g. Ribe and Davaille, 2013; Wouter et al., 2016). Though qualitative similar mechanisms
409 act in nature the dynamic similarity is hard to verify. Pressure in the model is controlled by the applied intrusion
410 rate and decreases over an experimental run as the intrusion rate is kept constant while the volumetric
411 fraction added to the growing intrusion decreases with $1/t$ systematically. Given the geometric and kinematic
412 similarities described above we suspect a realistic de-pressurization scenario in the model. However, given
413 the lack of quantitative observations in nature a conclusion remains elusive. Buoyancy in the model is likely
414 more important than in nature because the density ratio between PDMS and sand is low (1:1.7) while it may
415 be closer to equality (1:1) or even >1 (negatively buoyant) in nature, depending on magma composition. As
416 we observe silicone dikes intruding the overburden in a similar fashion as in nature (e.g. roof dikes, see
417 below), we suspect however, that buoyancy driven intrusion (i.e. diapirism) mimics residual melt injection
418 driven by local pressure anomalies in the prototype.

419 4.2 Comparison with previous results

420 4.2.1 Controlling parameters on pluton emplacement

421 In this study, the timing of the magmatic emplacement with respect to the regional tectonic deformation is
422 inferred as a controlling parameter on the finite pluton geometry and emplacement mode. Parallel, the shape
423 of the produced intrusions, based on the timing of their emplacement, is suggested as an effective diagnostic
424 feature. Notably, the findings of this work extend the results of previous studies that observed and described
425 experiments restricted under reference conditions (static, shear deformation) and processes of syn-tectonic
426 magmatic emplacement.

427 Based on our observations, the pluton emplacement is directly controlled by the syn-active evolving faults,
428 for both groups in pre- and syn-tectonic scenarios. At the same time, strain localization on the weak body
429 influences the upward fault propagation. Post-tectonic models are influenced and overprinted by the
430 boundary conditions and indirectly by the inherited fault structures during their emplacement. According to
431 our observations and in agreement with previous related studies (Román-Berdiel et al., 1997; 2000; Corti et
432 al., 2005) local interactions between on-going fault propagation and magma uprising induce asymmetric
433 intrusion shapes. In addition, the thickness ratio between the brittle and ductile band, influence the
434 interactions between the intrusive analogue magma and the developing model surface fault pattern. In our
435 case, the ratio between the ductile band (7mm) and the brittle layer thickness (40mm) is fixed at 0.175. This
436 ratio allows us to observe the overburden deformation without the fault pattern being completely overprinted
437 by deformations induced by piercement of the surface.

438 Román-Berdiel et al. (2000) pointed out the importance of the divergence angle, α , in deformation styles of
439 both surface and magma models, suggesting that for low values (i.e. $\alpha = 15^\circ$) under transtension the fault
440 pattern is similar to pure simple shear kinematics, therefore resulting in similar geometries for the syn-tectonic
441 intrusions. The fault structures observed in the reference experiments (RS and RT), during which no intrusion
442 takes place, are very similar to those described in previous experiments (e.g. Tchalenko, 1970; Wilcox et al.,
443 1973; Naylor et al., 1986). Moreover, for $\alpha < 30^\circ$, the deformation is mainly located in the central part of the
444 model and the localization of brittle deformation is very high (Román-Berdiel et al., 1999; 2000).

445 Previous studies have shown that variations in the displacement velocity and the intrusion rate control the
446 final geometry and orientation of the syn-tectonic magmatic body emplaced in the upper crustal layer
447 (Román-Berdiel et al., 1997; Corti et al., 2005). According to these studies, high horizontal-displacement or
448 low intrusion rates resulted in normal pluton asymmetry with the pluton's long axis parallelising the velocity
449 discontinuity (VD) zone, whereas low horizontal-displacement or high intrusion rates, generated plutons with
450 reverse asymmetry (magmatic emplacement controlled by tensional faults). In this study the variation of the
451 ratio between tectonic displacement rate and intrusion rate is constant. However, by varying the time of
452 emplacement we also captured observations on the pluton's asymmetry. Both pre-tectonic models show
453 normal pluton asymmetry, with the long pluton axis forming with the shear zone angles of $\theta = 28^\circ$ (Model A1;
454 Fig. 6c-d) and $\theta = 42^\circ$ (Model B1; Fig. 11c-d) and stretched to the extension direction. In the contrary, syn-

455 and post-tectonic models, from both experimental groups, show reverse asymmetry with their long axis
456 stretched to the compression direction, forming low angles with the shear zone (Fig. 6; Fig. 11f,i).

457 4.2.2 Interactions between deformation and pluton emplacement

458 The significant geometrical differences of the finite intrusions' shape observed among the emplacement
459 scenarios (Fig. 6; Fig. 11) reveal strong interactions between deformation and intrusion emplacement
460 (Román-Berdiel et al., 1997; Corti et al., 2005; Galland et al., 2007a; Montanari et al., 2010; Gomes et al.,
461 2019). Our experimental results, in both simple and transtensional shear settings, show that pre- and syn-
462 tectonic scenarios produce more elongated and fault-controlled intrusions in comparison to the less deformed
463 post-tectonic intrusions characterised by low aspect ratios. The presence of intrusion causes regional surface
464 uplift above the injection point and interferes with the fault structure evolution during their propagation.
465 Regarding the reference models, with no intrusion presence, fault-controlled pull-apart basin system and of
466 high subsidence rate occur for the transtensional group. The simple shear deformation results in a low angle
467 main deformed linear zone formed by low angle shears and anastomosing shear lenses. Exception to this
468 topography is Model A2 that resulted in narrow pull-apart system divided and displaced by the MF (Fig. 4e).

469 In accordance to the study of Gomes et al. (2019), this study illustrates that the shear zone deformation can
470 be significantly modified by rheological heterogeneities by looking at the shear zone perturbation effect arising
471 from passive (pre-tectonic) viscous-weak bodies. The pre-tectonic plutons, A1 and B1, with the gradual
472 evolution of the post-emplacement shearing start to accumulate strain deformation in a ductile manner
473 acquiring a sigmoidal (initially circular) shape of high aspect ratio and the lowest amplitude among all models
474 (Fig. 6a-d; Fig. 11 a-d). This is very well shown from the shape analysis, where the lower levels of these
475 intrusions are subparallel to the shear zone while the highest levels follow the finite stretching direction (Fig.
476 6c-d; Fig. 11, c-d). The surface structures observed only for this model are acting separately over the domal
477 uplift and not as one master fault (Fig. 3f). These above results seem compatible with the inferred observation
478 on caldera collapse modelling and the case of strike-slip deformation of brittle layer containing a passive
479 magmatic chamber (Holohan et al., 2008), where the magmatic chamber showed a NE-SW pluton axis
480 orientation, stretched approximately parallel to the extensional direction (in accordance to current study
481 Models A1 and B1). The limitation of pre-tectonic models, by the fault structures developing subparallel to
482 the boundary of the shear zone is an observation that is only attributed to the variations on the overburden
483 thickness (Román-Berdiel et al., 1997). The presence of the weak body delays the upward propagation of the
484 synthetic Riedel shears and results in a wider shear zone, in respect to its reference model (Fig. 2f; Fig. 3f).
485 Fact that is inferred from the deformational response and the delay of the shear zone formation on the brittle
486 surface, in comparison to the reference models (Fig. 2; Fig. 3; Fig.8).

487 In the case of the syn-tectonic intrusions, direct and strong interactions are developing among fault
488 propagation and magma ascent. Faults control and confine the emplacement of the intrusions, resulting in
489 narrow and acute pluton shape that follows the highly active master fault (e.g. Román-Berdiel et al., 1997,
490 Corti et al., 2005, Mazzarini et al., 2010). Syn-tectonic models in simple shear deformation show the highest

491 pluton amplitude among all models ($A_{A2} = 0.6$; Table 3). From the shape analysis of the excavated intrusions
492 is inferred local fault control on the intrusions' boundaries and orientation. Models A2 and B2, are initially
493 orientated subparallel to the shear zone (intrusions' lower level), with very low long axis angles. The deviation
494 of their deformational is registered at their highest levels when Model A2 seems to follow the Riedel
495 orientation (Fig. 6h) while Model B2 is oriented subparallel to σ_1 .

496 The post-tectonic intrusions, Models A3 and B3, ascend without being exposed to the stress field, besides
497 the push from below during their ascent. The shape analysis reveals a characteristic subcircular intrusion, of
498 an intermediate amplitude ($A_{A3} = 0.55$; $A_{B1} = 0.5$; Table 3) and with an analogous axis orientation to the syn-
499 tectonic models (Fig. 6k-l; Fig. 11k-l). Only from the strain analyses it is inferred that in both settings, the
500 uprising intrusions interferes and reactivates the pre-existing brittle structures (Fig. 5c; Fig. 10c).

501 As a second order feature, the dike system overprinting the intrusions, is observed and analysed upon
502 excavation. Diking occurs locally and along fault structures and for all models, is developing either on the
503 intrusion's flat roof top, as in the cases of pre- and post-tectonic emplacement models (Fig. 6a-b, i-j; Fig. 11a-
504 b, i-j) or as a form of a sheared tail intrusion's extension, as in the case of the syn-tectonic A2 and B2 Models
505 (Fig. 6e-f; Fig 11e-f).

506 Our models have shown that the pluton's geometry functions as an excellent first order discriminator for the
507 timing of the intrusion with respect to tectonic activity (Table 3). In addition, this study offers insights on the
508 surface deformation, which during field studies is limited due to the occurrence of natural (e.g. erosion) and
509 tectono-magmatic processes above most of the cases and outcropping intrusions. The diagnostic attributions
510 are summarized in Table 3.

511 4.3 Comparison with nature

512 Analogue modelling may be characterised by strong limitations and simplifications, mainly related to the
513 inability to reproducing natural thermal and rheological conditions. In addition, limitations on direct
514 comparison among natural and analogue models may be due to restricted exposure of plutons. From our
515 observations, the spatial and temporal relationships between emplacement-related structures and intrusion
516 vary with the level of the exposure. Analogue modelling studies have managed to reproduce models with
517 similar geometrical features of the plutons in the upper crustal levels, for different tectonic settings, supporting
518 the field evidences on tectonic control during pluton emplacement (Castro, 1987; Hutton, 1988) and testifying
519 the reliability of this modelling approach (Román-Berdiel et al., 1997; 2000; Galland et al., 2003; Corti et al.,
520 2005; Gomes et al., 2019).

521 The current analogue modelling approach provides new insights on the reliability of the finite pluton shape
522 as a diagnostic key-feature for constraining the temporal timing (pre-, syn- and post-tectonic) and spatial
523 conditions (tectonic setting) of the shallow crustal level emplacement. To validate our experimental
524 observables, we test them along with some second-order attributes against six cases of well-defined natural
525 examples, emplaced in simple shear and transtensional zones (Fig.13).

526 4.3.1 Natural examples of intrusions along simple shear zones

527 *The pre-tectonic Teixeira Pluton* (Fig. 13a,d) – This elongated ENE-trending batholith (80 km x 25 km)
528 is situated in NE Brazil and within a zone that is defined by the E-trending Patos, the So Josèdos Cordeiros
529 and the Juru shear zones (Fig.13a). The pre-tectonic Teixeira batholith is a leucocratic granite to quartz-
530 syenite in composition that shows a crystallization age of 591 ± 5 Ma (Zircon U/Pb). The batholith fabrics,
531 determined by anisotropy of magnetic susceptibility (AMS) and mineral shape preferred orientation, support
532 a pre-transcurrent batholith emplacement scenario (Archanjo et al., 2008). This natural example carries
533 similar features to the pre-tectonic Model A1 of this study (Fig. 6a-d). The pluton is characterised by high
534 aspect ratio ($L/W > 5$), with the long axis orientated subparallel to the extensional direction, forming an angle
535 of $\alpha = 15^\circ$. The Teixeira pluton, on map view, is elongated in a northeast-southwest direction, consistent with
536 the dextral pure strike-slip motion (Fig.13a).

537 Another natural example with similar characteristics to the pre-tectonic model A1 is the granitic Tazenakht
538 Pluton in Morocco. The pluton's deformation follows its emplacement within a left lateral strike slip fault,
539 running along its northern side (Ennih and Liegeois, 2001; Gasquet et al., 2008). The boundaries developing
540 between the fault structure and the intrusion boundaries are sharp. The pluton was probably subject to a
541 minor rotation during the deformational post-intrusion event. This natural example is characterised by high
542 axis ratio ($L/W = 1.6$) and the pluton's long axis forms an angle of $\alpha = 29^\circ$ with the shear zone. The local
543 presence of dykes and the geometrical features of the pluton are similar to those observed for the Model A1.

544 *The syn-tectonic Cabeza de Araya Pluton* (Fig. 13b, e) –The plutons of the Central Extremadura
545 batholith in the Iberian Massif (Fernández and Castro, 1999; Fig. 13b, e) is a natural example of syn-tectonic
546 plutonism. This natural example was imposed to tectonic deformation during its emplacement, triggered by
547 a right-lateral shear zone (Vignerresse and Bouchez, 1997; Fernández and Castro 1999; Corti et al., 2005).
548 The emplacement mode of the pluton is coeval with the dextral regional shear zone (Castro, 1985). The
549 pluton shows an aspect ratio of $L/W = 2.7$, with the long axis forming an angle of $\alpha = -45^\circ$ parallel to the
550 compression direction (NW-SE direction; Fig. 13b). Similarly, an intermediate axis ratio is observed for the
551 syn-tectonic Model A2 ($r = 2.5$; Fig. 6g, h). The model's long axis that corresponds to the higher contour
552 levels is orientated with the angle of ($\theta = -10^\circ$), making this natural model a prototype for this emplacement
553 scenario.

554 In addition to this, there are also other important natural examples of syn-tectonic intrusion emplacement
555 scenarios that shows similarities to our observations: 1) *Karawanken pluton* (Visonà and Zanferrari 2000;
556 Rosenberg 2004); 2) *The Lizio pluton* (Román-Berdiel et al., 1997; Fernandez and Castro 1999; Corti et al.,
557 2005); 3) Cases of Syn-tectonic magmatism along the Periadriatic Fault System (Rosenberg, 2004).

558 *The post-tectonic Vila Pouca de Aguiar pluton* (Fig. 13c, f) – This is a natural example of a post-
559 tectonic granitic intrusion that is emplaced after the main left-lateral shear phase event (Fig. 13c; Sant'Ovaia
560 et al., 2000). It is suggested that the first to be emplaced and the least evolved granite type (Vila Pouca de
561 Aguiar Granite) upwelled from the local, NE-trending fault-zone, acting as a dike, and formed a thin sill where

562 NE-directed magma flow was dominant. In this case, the pre-existing features exert a major role during
563 emplacement leading to the roughly alignment of the intrusion with the shear zone ($\alpha = -4^\circ$, Fig.13f), with the
564 pluton axis parallel to the compression direction. Even if the pre-tectonic group generated intrusions with the
565 lowest aspect ratios ($r < 1.5$; Fig. 7), the intrusion ellipses corresponding to higher contour levels resulted in
566 a similar aspect ratio ($r = 1.9$) and elongated shape to the *Vila Pouca de Aguiar* pluton (Fig. 6l).

567 Another characteristic natural example of post-tectonic emplacement is the Águas Frias (AF) pluton (Martins
568 et al., 2009; Fig. 13c). This post-tectonic granitic pluton, situated NE from the Vila Pouca de Aguiar pluton,
569 occupies an area of 30 km² and is associated with Penacova-Régua-Verin fault (PRVF) that belongs to the
570 NNE-trending brittle system crosscutting the whole Northern Portugal. Its emplacement was fed through a
571 deep conduit located at the centre of the pluton. VPA and AF plutons, similar in mineralogical, chronological
572 and magnetic features, are joined together at depth and were fed through feeding zones located within the
573 NNE-SSW Penacova-Régua -Verin Fault.

574 4.3.2 Natural examples for intrusion into transtensional shear zones

575 *The pre-tectonic Eğrigöz pluton* (Fig. 13g,i) - This natural example regards a N-S elongated (40x15
576 km) granite body (20.5 ± 1.1 - 18.9 ± 1.2 Ma.; Catlos, et al., 2012), situated in the northern Menderes
577 metamorphic core complex and covering an area of 330 Km². Its geometrical features show a high aspect
578 ratio of $L/W = 2.6$ and an axis trend of $\alpha = 46^\circ$ (parallel to the extension direction), analogous to the
579 observations made for the higher contour levels of the strongly deformed pre-tectonic Model B1 ($r = 1.9$; $\theta =$
580 42° ; Fig.11d; Table 3). The 20km-long, NE-striking Gerni shear zone is closely linked to the pulses of
581 magmatic activity and it is assumed to have propagated immediately following the emplacement of the
582 Eğrigöz pluton. Stress tensor results of the Eğrigöz pluton indicate that the shear zone has been predominant
583 under NE-SW-trending extension. The presence of the aplitic and pegmatitic dikes along the periphery and
584 structurally upper parts of the pluton (Erkül et al. 2017) are rather common and similarly reproduced during
585 the analogue Model B1 experiment (Fig. 11a-b).

586 In addition to this example, other plutons are registered carrying similar diagnostic features of pre-tectonic
587 emplacement mode: 1) *The Totoltepec Pluton* (Kirsch et al. 2013); 2) *The Devonian granitoid of Pampa de*
588 *Achala*, in Central Argentina (Simpson et al. 2001); 3) *The Koyunoba pluton* (Erkül et al. 2017).

589 *The syn-tectonic Monzoni Intrusive Complex* (Fig.13h, k) – This 4 km-long intrusion situated in the central
590 Dolomites in Italy offers a great occasion for comparison due to its excellent three-dimensional exposure.
591 However and mainly due to contact metamorphism around the pluton and the syn-metamorphic thermally
592 driven fluid circulation, field observations are very limited, and still there is very poor knowledge of kinematic
593 indications. Based on analogue modelling observations, new insights on the shear zone and fault structures,
594 of the missing upper crustal layer that once hosted the emplaced magmatic chamber, is achieved. It is
595 assumed that the pluton's emplacement mode is controlled by the Middle Triassic tectonics, however the
596 time of emplacement (syn-tectonic or indirect post-tectonic emplacement) along the left-lateral shear zone is
597 still under discussion. According to our model observations, this pluton exhibits diagnostic characteristics

598 similar to a syn-to late tectonic intrusion (Abbas et al., 2018). The pluton's long axis trends with an angle of
599 $\alpha = -14^\circ$, parallel to the compressional field, and shows an aspect ratio of $L/W = 2$ (Fig. 13k). The shape
600 analysis of this pluton shows similarity to the Model B2 ($-10 < \theta < -19^\circ$; $r = 1.7$; Fig.11g-h). The syn-magmatic
601 dike swarms, cropping out at the intrusion area, appear to cut the deformed sedimentary country rocks and
602 intrude the magmatic edifice (Sloman 1989; Bonadiman et al., 1994; Gianolla et al., 2010) while the pluton
603 carries a NE–SW striking apophysis that trails the intrusion at its SW boundary.

604 Similar natural examples of syn-tectonic emplacement mode are: 1) *The Mortagne pluton* (Román-Berdiel et
605 al.,1997); 2) *The Los Pedroches pluton* (Aranguren et al. 1997; Román-Berdiel et al.,2000); 3) *The Jihlava*
606 *Intrusion* (Verner et al. 2006); 4) *The Hombreiro pluton* (Román-Berdiel et al.,2000); 5) *The Gulf of Aden*
607 *Ridge* (Corti et al. 2003).

608 *The post-tectonic La Tojiza Pluton* (Fig. 13i,l) - The La Tojiza granite is cropping out in the Mondonẽdo
609 Nappe Domain (Fig. 13c) and according to geochronological data it consists with a U–Pb age of 295 ± 2 Ma
610 (Fernández-Suárez et al. 2000). This post-tectonic association is composed of granite–granodiorite–tonalite–
611 monzogranite intrusions. The intrusion reactivated the inherited transtensional tectonic structures, leading to
612 the emplacement and formation of a sub-circular pluton of 16 km-diameter (Aranguren et al., 2003). Its
613 thickness is estimated of 1 km and the root zone is located at its eastern border. The pluton shows an axis
614 trend of $\alpha = -6^\circ$ and parallel to the compressional field, with the pluton's aspect ratio $L/W = 1.2$ (Fig. 13l).
615 Most of the observed aplitic dikes are present on the roof of the pluton and oblique to the magnetic lineation.
616 These features are in great accordance with the lower contour levels of the post-tectonic Model B3 ($\theta = 0^\circ$; r
617 $= 1.4$; Fig. 11k-l).

618 The *Plasenzuela Intrusion* (Central Extremadura, Spain; Fernandez and Castro 1999) represents another
619 natural example for this emplacement scenario, characterised by a well-defined rounded pluton shape of low
620 aspect ratio ($L/W \sim 1$).

621 4 Conclusions

622 This study provides new insights on the application of the finite pluton shape as a diagnostic indicator for
623 constraining the tectonic setting and the relative timing of magma emplacement versus tectonics. Three
624 scenarios on pluton emplacement (pre-, syn- and post-tectonic) in two different tectonic settings (simple
625 shear, transtension) are tested and analysed. The intrusion shapes (aspect ratio, principal axis trend,
626 amplitude) and the model surface deformation are measured and described, providing useful insights for the
627 understanding of the interactions occurring between tectonics and magmatism. The main insights and
628 conclusions supported by this study are the following:

- 629 1. Incremental strain analysis and final surface deformation reveal a different deformational pattern
630 among the scenarios and strong interactions between tectonics and magma emplacement. Pre-
631 tectonic models accumulate regional strain during shearing, resulting in the delay and diffusion of

632 the brittle structures during their up-ward propagation. Here, the final shear zone appears wider than
633 the respective reference model and crosscut but more than one well-defined fault. Syn-tectonic
634 emplacement causes the major boundary faults to extend and curve towards the centre and the
635 formation of a narrow fault-controlled pull-apart basin overprinted by the master fault. The inverse
636 shear sense, captured in strain maps, caused during intrusion is observed exclusively in the post-
637 tectonic scenario.

638 2. The final shape of the intrusions, emplaced along shear zones with a different timing respect to the
639 tectonic activity, show significant deformational variations, delineating its reliability as a diagnostic
640 feature. Observations coming from both tectonic groups (simple shear and transtension) infer
641 parallel deformational pattern and geometrical characteristics for the intrusions of similar timing of
642 emplacement (pre-, syn- or post-tectonic). Based on the analytical shape analysis, the asymmetric
643 and deformed final intrusions reflect the regional stresses and finite strain field. The axis aspect ratio
644 and trend are evolving against the contour level for each model, remaining consistent among those
645 emplaced coevally.

646 3. Among the emplacement scenarios, the pre-tectonic intrusions appear strongly elongated parallel
647 to the extension field with the lowest amplitude and the highest aspect ratios. The intrusion's flat top
648 is overprinted by post-emplacement shears. Syn-tectonic models are characterised by high
649 amplitude and moderate aspect ratios. They bear acute roofs, oriented parallel to the compression
650 direction, and scissor-tail apophysis that trails the intrusion. The sub-circular post-tectonic models
651 show the lowest aspect ratios and a similar orientation to syn-tectonic models.

652 4. Faults that crosscut the central zone overprint the emplaced or up-lifting intrusion, navigating the
653 intrusions' margins and serving as pathway for diking. The higher levels of the syn- and post-tectonic
654 intrusion boundaries appear parallel to and constrained by the synthetic faults developing on the
655 surface. The lateral expansion of pre-tectonic models is bounded by the major fault structures
656 developing subparallel to the boundary of the shear zone, while their top is overprinted by roof-diking
657 guided by crosscutting shears.

658 5. The obtained diagnostic attributes are tested successfully against natural prototypes, confirming the
659 diagnostic potential and reliability of the intrusion's shape for constraining the time and the tectonic
660 setting of the magmatic emplacement.

662 5 Acknowledgments

663 The experiments were performed at the HelTec - Helmholtz Laboratory for Tectonic Modelling of the
664 Helmholtz Centre Potsdam - German Research Centre for Geosciences (GFZ), in Potsdam (Germany). The
665 authors wish to thank F. Neumann and T. Ziegenhagen (GFZ German Research Centre for Geosciences)

666 for their technical support and engineering. T. Román-Berdiel for her valuable reviews on a previous version
667 of the manuscript, as well as E. Carminati (*Sapienza University*), M. Mattei (*Roma Tre University*) and C.
668 Bonadiman (University of Ferrara) for their constructive discussions and contributions. Part of this research
669 was funded by the IUSS-PhD mobility grant (University of Ferrara). The research has been supported by the
670 Deutsche Forschungsgemeinschaft (DFG) through CRC1114 "Scaling Cascades in Complex Systems",
671 Project B01 and EPOS – the European Plate Observing System.

672 6 References

- 673 Abbas, H., Michail, M., Cifelli, F., Mattei, M., Gianolla, P., Lustrino, M., Carminati, E., 2018. Emplacement
674 modes of the Ladinian plutonic rocks of the Dolomites: Insights from anisotropy of magnetic susceptibil-
675 ity. *J. Struct. Geol.* 113, 42-61.
- 676 Adam, J., Urai, J.L., Wieneke, B., Oncken, O., Pfeiffer, K., Kukowski, N., Lohrmann, J., Hoth, S., Van der
677 Zee, W., Schmatz, J., 2005. Shear localisation and strain distribution during tectonic faulting - new in-
678 sights from granular-flow experiments and high-resolution optical image correlation techniques. *J.*
679 *Struct. Geol.* 27, 283-301. doi: 10.1016/j.jsg.2004.08.008.
- 680 Aranguren, A., Cuevas, J., Tubia, J.M., Román-Berdiel, T., Casas-Sainz, A., Casas-Ponsati, A., 2003. Gran-
681 ite laccolith emplacement in the Iberian arc: AMS and gravity study of the La Tojiza pluton (NW Spain).
682 *J. Geol. Soc. London.* 160, 435–445. doi:10.1144/0016-764902-079
- 683 Bartlett, W.L., Friedman, M., Logan, J.M., 1981. Experimental folding and faulting of rocks under confining
684 pressure Part IX. Wrench faults in limestone layers. *Tectonophysics* 79, 255–277. doi:10.1016/0040-
685 1951(81)90116-5.
- 686 Benn, K., Odonne, F., De Saint Blanquat, M., 1998. Pluton emplacement during transpression in brittle crust:
687 New views from analogue experiments. *Geology* 26, 1079–1082. doi:10.1130/0091-
688 7613(1998)026<1079: PEDTIB>2.3.CO.
- 689 Benn, K., Odonne, F., Lee, S.K.Y., Darcovich, K., 2000. Analogue scale models of pluton emplacement dur-
690 ing transpression in brittle and ductile crust. *Trans. R. Soc. Edinb. Earth Sci.* 91, 111–121. doi:10.1130/O-
691 8137-2350-7.111.
- 692 Bonadiman, C., Coltorti, M., Siena, F., 1994. Petrogenesis and T-fO₂ estimates of Mt. Monzoni Complex
693 (central Dolomites, Southern Alps); a Triassic shoshonitic intrusion in a transcurrent geodynamic setting.
694 *Eur. J. Mineral.* 6, 943–966.
- 695 Brown, M., 2013. Granite: From genesis to emplacement. *Geol. Soc. Am. Bull.* 125, 1079–1113.
696 doi:10.1130/B30877.1.
- 697 Burov, E., Jaupart, C., and Guillou-Frottier, L., 2003. Ascent and emplacement of buoyant magma bodies in
698 brittle-ductile upper crust. *J. Geophys. Res.* 108. doi: 10.1029/2002JB001904
- 699 Catlos, E. J., Jacob, L., Oyman, T., & Sorensen, S., 2012. Long-term exhumation of an Aegean metamorphic
700 core complex granitoids in the Northern Menderes Massif, western Turkey. *American Journal of Sci-*
701 *ence*, 312(5), 534-571.
- 702 Castro, A., Fernández, C., 1998. Granite intrusion by externally induced growth and deformation of the
703 magma reservoir, the example of the Plasenzuela pluton, Spain. *J. Struct. Geol.* 20, 1219–1228.
704 doi:10.1016/S0191-8141(98)00056-X

- 705 Corti, G., Bonini, M., Conticelli, S., Innocenti, F., Manetti, P., Sokoutis, D., 2003. Analogue modelling of con-
706 tinental extension: A review focused on the relations between the patterns of deformation and the pres-
707 ence of magma. *Earth-Science Rev.* 63, 169–247. doi:10.1016/S0012-8252(03)00035-7
- 708 Corti, G., Moratti, G., Sani, F., 2005. Relations between surface faulting and granite intrusions in analogue
709 models of strike-slip deformation. *J. Struct. Geol.* 27, 1547–1562. doi:10.1016/j.jsg.2005.05.011
- 710 De Saint Blanquat, M., Horsman, E., Habert, G., Morgan, S., Vanderhaeghe, O., Law, R., Tikoff, B., 2011.
711 Multiscale magmatic cyclicality, duration of pluton construction, and the paradoxical relationship between
712 tectonism and plutonism in continental arcs. *Tectonophysics* 500, 20–33.
713 doi:10.1016/j.tecto.2009.12.009
- 714 Dooley, T.P., Schreurs, G., 2012. Analogue modelling of intraplate strike-slip tectonics: A review and new
715 experimental results. *Tectonophysics* 790, 574-575, 1–71. <https://doi.org/10.1016/j.tecto.2012.05.030>.
- 716 Erkül F., Erkül, S.T., Manap, H.S., Çolak, C., 2017. An extensional and transtensional origin of elongated
717 magmatic domes and localised transfer faults in the northern Menderes metamorphic core complex,
718 western Turkey. *Geodinamica Acta* 29, 139-159. doi:10.1080/09853111.2017.1343523
- 719 Ennih, N., Liégeois, J.P., 2001. The Moroccan Anti-Atlas: The West African craton passive margin with limited
720 Pan-African activity. Implications for the northern limit of the craton. *Precambrian Res.* 112, 289–302.
721 doi:10.1016/S0301-9268(01)00195-4
- 722 Fernández, C., Castro, A., 1999. Pluton accommodation at high strain rates in the upper continental crust.
723 The example of the Central Extremadura batholith, Spain. *J. Struct. Geol.* 21, 1143–1149.
724 doi:10.1016/S0191-8141(99)00086-3
- 725 Fernández, C., Castro, A., 1999. Pluton accommodation at high strain rates in the upper continental crust.
726 The example of the Central Extremadura batholith, Spain. *J. Struct. Geol.* 21, 1143–1149.
727 doi:10.1016/S0191-8141(99)00086-3
- 728 Fernández-Suárez, J., Dunning, G.R., Jenner, G.A., and Gutiérrez-Alonso, G., (2000). Variscan collisional
729 magmatism and deformation in NW Iberia: constraints from U-Pb geochronology of granitoids. *Journal*
730 *of the Geological Society*, 157, 565-576.
- 731 Ferré, E.C., Galland, O., Montanari, D., Kalakay, T.J., 2012. Granite magma migration and emplacement
732 along thrusts. *Int. J. Earth Sci.* 101, 1673–1688. doi:10.1007/s00531-012-0747-6.
- 733 Fossen, H., Teyssier, C., Whitney, D.L., 2013. Transtensional folding. *J. Struct. Geol.* 56, 89–102.
734 doi:10.1016/j.jsg.2013.09.004.
- 735 Galland, O., Holohan, E., van Wyk de Vries, B., Burchardt, S., 2015. Laboratory Modelling of Volcano Plumbing
736 Systems: A Review. In: Breikreuz C., Rocchi S. (eds) *Physical Geology of Shallow Magmatic Sys-*
737 *tems. Advances in Volcanology.* Springer, 1-68 doi:10.1007/11157_2015_9.
- 738 Galland, O., Cobbold, P.R., de Bremond d’Ars, J., Hallot, E., 2007b. Rise and emplacement of magma during
739 horizontal shortening of the brittle crust: Insights from experimental modeling. *J. Geophys. Res. Solid*
740 *Earth* 112, 1–21. doi:10.1029/2006JB004604.
- 741 Galland, O., Cobbold, P.R., Hallot, E., de Bremond d’Ars, J., Delavaud, G., 2006. Use of vegetable oil and
742 silica powder for scale modelling of magmatic intrusion in a deforming brittle crust. *Earth Planet. Sci.*
743 *Lett.* 243, 786–804. doi:10.1016/j.epsl.2006.01.014.
- 744 Galland, O., de Bremond d’Ars, J., Cobbold, P.R., Hallot, E., 2003. Physical models of magmatic intrusion
745 during thrusting. *Terra Nova* 15, 405–409. doi:10.1046/j.1365-3121.2003.00512.x.

- 746 Galland, O., Hallot, E., Cobbold, P.R., Ruffet, G., de Bremond d'Ars, J., 2007a. Volcanism in a compressional
747 Andean setting: A structural and geochronological study of Tromen volcano (Neuquén province, Argen-
748 tina). *Tectonics* 26. doi:10.1029/2006TC002011.
- 749 Gasquet, D., Ennih, N., Liegeois, J.P., Soullaimani, A., Michard, A., 2008. The Pan-African Belt, in: *Continental
750 Evolution: The Geology of Morocco. Lecture Notes in Earth Sciences*. 33–64.
- 751 Gomes, A.S., Rosas F.M., Duarte J.C., Schellart W.P., Almeida J., Tomás, R., Strak, V., 2019. Analogue
752 modelling of the brittle shear zone propagation across upper crustal morpho-rheological heterogeneities.
753 *J. Struct. Geol.* 126, 175–197. doi: 10.1016/j.jsg.2019.06.004.
- 754 Handy, M.R., Mulch, A., Rosenau, M. and Rosenberg, C. L., 2001. The role of fault zones and melts as
755 agents of weakening, hardening and differentiation of the continental crust: a synthesis. *Geol. Soc. Spec.
756 Publ.*, 186, 305–332. doi:10.1144/GSL.SP.2001.186.01.18.
- 757 Handy, M.R., Streit, J.E., 1999. Mechanics and mechanisms of magmatic underplating: Inferences from mafic
758 veins in deep crustal mylonite. *Earth Planet. Sci. Lett.* 165, 271–286. doi:10.1016/S0012-
759 821X(98)00272-6.
- 760 Holohan, E.P., Van Wyk de Vries, B., Troll, V.R., 2008. Analogue models of caldera collapse in strike-slip
761 tectonic regimes. *Bull. Volcanol.* 70, 773–796. <https://doi.org/10.1007/s00445-007-0166-x>. Hubbert,
762 M.K., 1937. Theory of scalable models as applied to the study of geologic structures. *Geol. Soc. Am.
763 Bull.* 48, 1459–1520. doi:10.1130/GSAB-48-1459.
- 764 Hutton, D.H.W., Reavy, R.J., 1992. Strike-slip tectonics and granite petrogenesis. *Tectonics* 11, 960–967.
765 doi:10.1029/92TC00336.
- 766 Hutton, D.H.W., 1988. Granite emplacement mechanisms and tectonic controls: inferences from deformation
767 studies. *Trans. R. Soc. Edinb. Earth Sci.* 79, 245–255. doi:10.1017/S0263593300014255.
- 768 Kirsch, M., Keppie, J.D., Murphy, J.B., Lee, J.K.W., 2013. Arc plutonism in a transtensional regime: The late
769 Palaeozoic Totoltepec pluton, Acatlán Complex, southern Mexico. *Int. Geol. Rev.* 55, 263–286.
770 doi:10.1080/00206814.2012.693247.
- 771 Klinkmüller, M., Schreurs, G., Rosenau, M., Kernitz, H., 2016. Properties of granular analogue model ma-
772 terials: A community wide survey. *Tectonophysics* 684, 23–38. doi:10.1016/j.tecto.2016.01.017.
- 773 Koptev, A., Burov, E., Gerya, T., Le Pourhiet, L., Leroy, S., Calais, E., Jolivet, L., 2017. Plume-induced con-
774 tinental rifting and break-up in ultra-slow extension context: Insights from 3D numerical modeling. *Tec-
775 tonophysics*. Article in press. doi:10.1016/j.tecto.2017.03.025.
- 776 Mandal, N., Chakraborty, C., 1990. Strain fields and foliation trajectories around pre-, syn-, and post-tectonic
777 plutons in coaxially deformed terranes. *Geol. J.* 25, 19–33. doi:10.1002/gj.3350250103.
- 778 Mazzarini, F., Musumeci, G., Montanari, D., Corti, G., 2010. Relations between deformation and upper crustal
779 magma emplacement in laboratory physical models. *Tectonophysics* 484, 139–146.
780 doi:10.1016/j.tecto.2009.09.013.
- 781 Montanari, D., Corti, G., Sani, F., Del Ventisette, C., Bonini, M., Moratti, G., 2010. Experimental investigation
782 on granite emplacement during shortening. *Tectonophysics* 484, 147–155.
783 doi:10.1016/j.tecto.2009.09.010.
- 784 Paterson, S.R., Okaya, D., Memeti, V., Economos, R., Miller, R.B., 2011. Magma addition and flux calcula-
785 tions of incrementally constructed magma chambers in continental margin arcs: Combined field, geo-
786 chronologic, and thermal modeling studies. *Geosphere* 7, 1439–1468. doi:10.1130/GES00696.1.

- 787 Paterson, S.R., Schmidt, K.L., 1999. Is there a close relationship between faults and plutons? *J. Struct. Geol.*
788 21, 1131–1142.
- 789 Paterson, S.R., Tobisch, O.T., 1988. Using pluton ages to date regional deformations: problems with com-
790 monly used criteria. *Geology* 16, 1108–1111.
- 791 Petford, N., Cruden, A.R., McCaffrey, K.J., Vigneresse, J.-L., 2000. Granite magma formation, transport and
792 emplacement in the Earth's crust. *Nature* 408, 669–673. doi:10.1038/35047000.
- 793 Ramberg, H., 1981. Gravity, deformation and the Earth's crust: In *Theory, Experiments, and Geological Ap-*
794 *plication*. London, Academic Press, 452.
- 795 Ribe, N.M., Davaille, A., 2013. Dynamical similarity and density (non-) proportionality in experimental tecton-
796 ics. *Tectonophysics* 608, 1371–1379. doi: 10.1016/j.tecto.2013.06.005.
- 797 Riedel, W., 1929. Zur Mechanik geologischer Brucherscheinungen. *Zentralblatt Mineral., Geol. u. Paläont.*
798 B, 354–368.
- 799 Ritter, M.C., Leever, K., Rosenau, M., Oncken, O., 2016. Scaling the sandbox-Mechanical (dis) similarities
800 of granular materials and brittle rock. *Journal of Geophysical Research: Solid Earth*, 121(9), 6863–6879.
801 doi:10.1002/2016jb012915.
- 802 Román-Berdiel, T., 1999. Geometry of granite emplacement in the upper crust: contributions of analogue
803 modelling, in: Castro, A., Fernandez, C., Vigneresse, J.L. (Eds.), *Understanding granites: Integrating*
804 *new and classical techniques*. Geological Society, London, Special Publications. 168. 77–94.
805 doi:10.1144/GSL.SP.1999.168.01.06.
- 806
- 807 Román-Berdiel, T., Aranguren, A., Cuevas, J.L., Tubia, J.M., Gapais, D., Brun, J.-P., 2000. Experiments on
808 granite intrusion in transtension, in: Vendeville, B., Mart, Y., Vigneresse, J.L. (Eds.), *Salt, Shale and*
809 *Igneous Diapirs in and around Europe*. Geological Society, London, Special Publications. 174. 21–42.
810 doi:10.1144/GSL.SP.1999.174.01.02.
- 811 Román-Berdiel, T., Gapais, D., Brun, J.P., 1997. Granite intrusion along strike-slip zones in experiment and
812 nature. *Am. J. Sci.* 297, 651–678. doi:10.2475/ajs.297.6.651.
- 813 Rosenberg, C.L., 2004. Shear zones and magma ascent: A model based on a review of the Tertiary magma-
814 tism in the Alps. *Tectonics* 23, 21. doi:10.1029/2003TC001526.
- 815 Rosenau et al. (2018): Ring-shear test data of quartz sand G12 used for analogue experiments in the Helm-
816 holtz Laboratory for Tectonic Modelling (HelTec) at the GFZ German Research Centre for Geosciences
817 in Potsdam. GFZ Data Services. doi:10.5880/GFZ.4.1.2019.003.
- 818 Rudolf, M., Boutelier, D., Rosenau, M., Schreurs, G., Oncken, O., 2016. Rheological benchmark of silicone
819 oils used for analog modeling of short- and long-term lithospheric deformation. *Tectonophysics* 684, 12–
820 22. doi:10.1016/j.tecto.2015.11.028.
- 821 Sant'Ovaia, H., Bouchez, J.L., Noronha, F., Leblanc, D., Vigneresse, J.L., 2000. Composite-laccolith em-
822 placement of the post-tectonic Vila Pouca de Aguiar granite pluton (northern Portugal): A combined
823 AMS and gravity study. *Trans. R. Soc. Edinb. Earth Sci.* 91, 123–137.
824 doi:10.1017/S026359330000732X.
- 825 Schellart, W.P., Strak, V., 2016. A review of analogue modelling of geodynamic processes: Approaches,
826 scaling, materials and quantification, with an application to subduction experiments. *J. Geodyn.* 100, 7-
827 32. doi:10.1016/j.jog.2016.03.009.

- 828 Schöpfer, M.P.J., Steyrer, H.P., 2001. Experimental modeling of strike-slip faults and the self-similar behavior. *Geol. Soc. Am. Mem.* 193, 21–27. doi:10.1130/0-8137-1193-2.21.
829
- 830 Schreurs, G., 2003. Fault development and interaction in distributed strike-slip shear zones: an experimental
831 approach, in: Storti, F., Holdsworth, R.E., Salvini, F. (Eds.), *Intraplate Strike-Slip deformation belts*. Geological Society, London, Special Publications. 35–52. doi:10.1144/GSL.SP.2003.210.01.03.
832
- 833 Shinevar, W.J., Behn, M.D., Hirth, G., 2015. Compositional dependence lower crustal viscosity, *Geophys.*
834 *Res. Lett.* 42, 8333–8340. doi:10.1002/2015GL065459.
- 835 Simpson, C., Whitmeyer, S.J., De Paor, D., Gromet, L.P., Miro, R., Krol, M., and Short, H., 2001. Sequential
836 ductile to brittle reactivation of major fault zones along the accretionary margin of Gondwana in Central
837 Argentina. In: Holdsworth, R.E. et al. (eds.) *The Nature and Tectonic Significance of Fault Zone Weakening*.
838 *Geol. Soc. London, Special Publications*, 186, 233-255.
- 839 Sloman, L., 1989. Triassic shoshonites from the Dolomites, northern Italy: alkaline arc rocks in a strike-slip
840 setting. *J. Geophys. Res.* 94, 4655–4666.
- 841 Verner, K., Žák J., Hrouda, F., Holub, F., 2006. Magma emplacement during exhumation of the lower- to mid-
842 crustal orogenic root: the Jihlava syenitoid pluton, Moldanubian Unit, Bohemian Massif. *J Struct Geol.*
843 28,1553–1567.
- 844 Vigneresse, J.L., 1995. Control of granite emplacement by regional deformation. *Tectonophysics* 249, 173–
845 186. doi:10.1016/0040-1951(95)00004-7.
- 846 Vigneresse, J.L., Bouchez, J.L., 1997. Successive Granitic Magma Batches During Pluton Emplacement: the
847 Case of Cabeza de Araya (Spain). *J. Petrol.* 38, 1767–1776. doi:10.1093/etroj/38.12.1767
- 848 Visonà, D., Zanferrari, A., 2002. Some constraints on geochemical features in the Triassic mantle of the
849 easternmost Austroalpine-Southalpine domain: evidence from the Karawanken pluton (Carinthia, Austria).
850 *International Journal of Earth Sciences*, 89 (2000), 40-51.
- 851 Weijermars, R., Schmeling, H., 1986. Scaling of Newtonian and non-Newtonian fluid dynamics without inertia
852 for quantitative modelling of rock flow due to gravity (including the concept of rheological similarity).
853 *Phys. Earth Planet. Inter.* 43, 316–330. doi:10.1016/0031-9201(86)90021-X
- 854 Westoby, M.J., Brasington, J., Glasser, N.F., Hambrey, M.J. & Reynolds, J.M., 2012. Structure-from-Motion
855 photogrammetry: A low-cost, effective tool for geoscience applications. *Geomorphology*, 179, 300-314.
856 doi:10.1016/j.geomorph.2012.08.021.
- 857 Wilcox, R.E., Harding, T.P., Seely, D.R., 1973. Basic wrench tectonics. *Am. Assoc. Pet. Geol. Bull.* 57, 74–
858 96. doi:10.1306/819A424A-16C5-11D7-8645000102C1865D.
- 859 Xiao, Y., Wu, G., Lei, Y., Chen, T., 2017. Analogue modeling of through-going process and development
860 pattern of strike-slip fault zone. *Pet. Explor. Dev.* 44, 368–376. doi:10.1016/S1876-3804(17)30043-5.
- 861

862 7 Tables

863

864 Table 1 Model characteristics and experimental conditions

Models	Thickness of brittle layer	Thickness of ductile layer	Intrusion rate, Ir	Injected Volume, Iv	Relative displacement rate, Dv	Total horizontal displacement, Dt	Experiment Duration
Reference models (Group R)							
Simple shear RS	40mm	7mm	-	-	1.0 mm/min	30 mm	30 min
Transtension RT	40mm	7mm	-	-	1.0 mm/min	30 mm	30 min
Static Intrusion R0	40mm	7mm	21.0 mm ³ /s	37.7x10 ³ mm ³	-	-	30 min
Simple shear models (Group A)							
Pre-tectonic intrusion A1	40mm	7mm	21.0 mm ³ /s	37.7x10 ³ mm ³	1.0 mm/min	30 mm	60 min
Syn-Tectonic Intrusion A2	40mm	7mm	21.0 mm ³ /s	37.7x10 ³ mm ³	1.0 mm/min	30 mm	30 min
Post-tectonic intrusion A3	40mm	7mm	21.0 mm ³ /s	37.7x10 ³ mm ³	1.0 mm/min	30 mm	60 min
Transtension models (Group B)							
Pre-tectonic intrusion B1	40mm	7mm	21.0 mm ³ /s	37.7x10 ³ mm ³	1.0 mm/min	30 mm	60 min
Syn-Tectonic Intrusion B2	40mm	7mm	21.0 mm ³ /s	37.7x10 ³ mm ³	1.0 mm/min	30 mm	30 min
Post-tectonic intrusion B3	40mm	7mm	21.0 mm ³ /s	37.7x10 ³ mm ³	1.0 mm/min	30 mm	60 min

865

866 **Table 2 Material properties and scaling factors**

Parameters	Models	Nature	Model/ Nature (Scaling factor)
Brittle material			
	Quartz Sand	Upper Crust	
Length, L	0.01 m	0.6 - 6 km	$0.6 - 6 \times 10^{-6}$
Cohesion, C	10-100 Pa	10 MPa	$1-10 \times 10^{-6}$
Density, ρ	1600 Kg/m	2600 kg/m	0.615
Gravity, g	9.81 m/s	9.81 m/s	1
Viscous material			
	Silicone oil	Intrusion/ shear zone	
Viscosity, η	3×10^4 Pa s	$>10^{18}$ Pa s	3.0×10^{-14}
Density, ρ	965 kg/m	1600 kg/m	0.603
Time, t	1 sec	30000 yrs	10^{-13}

867

868 **Table 3 Summarizing table of diagnostic attributes as suggested by the analogue models for the different em-**
 869 **placement scenarios.**

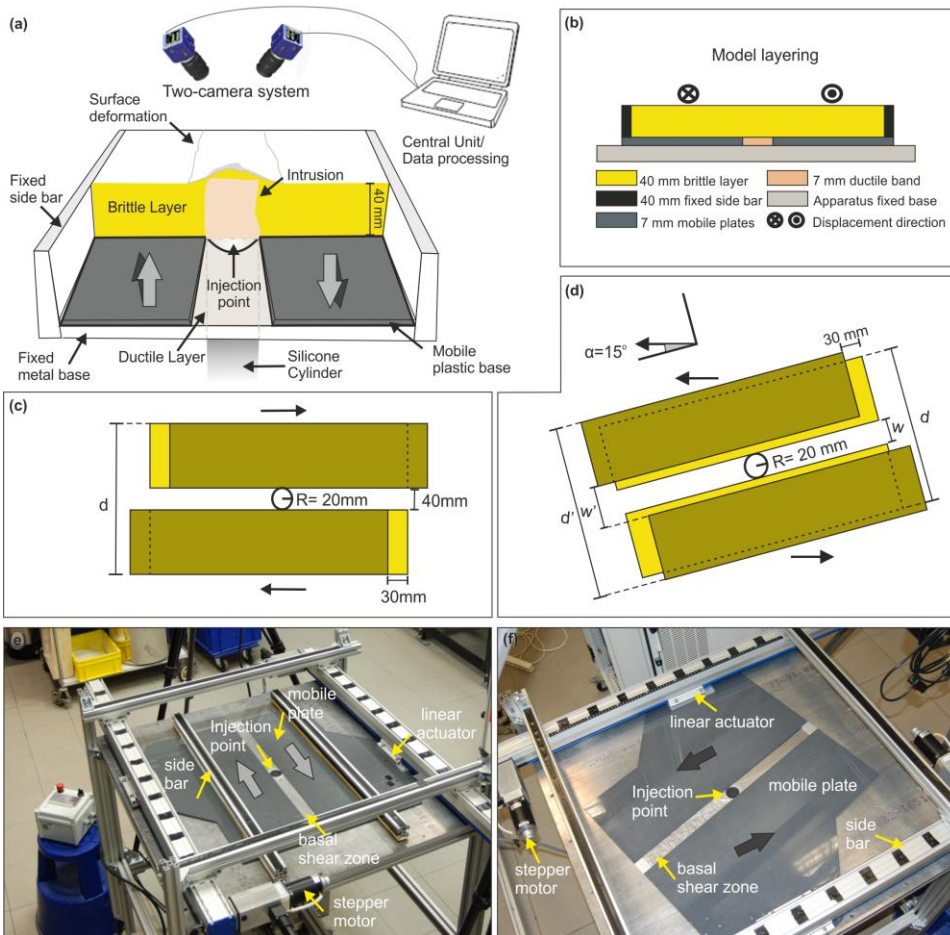
Model	Pluton Elongation #		Orientation #	Dike system	Pluton Amplitude, A
	Group A	Group B			
Pre-tectonic	High ($r_{A1} > 1.5$)	High ($r_{B1} > 1.5$)	Long axis // extension	Roof	Low
Syn-Tectonic	High ($r_{A2} > 1.5$)	* Medium/High ($r_{B2} > 1.5$)	Long axis // compression	Lateral (apophysis)	High
Post-tectonic	Low ($r_{A3} < 1.5$)	Low ($r_{B3} < 1.5$)	Long axis // compression	Roof	Medium

870 * Based on observations of repetition models (100, 59, 95; see Appendix)

871 # Based on an ellipse fitted to the lower (c_1) and higher (C_2) contour levels of the intrusions.

872 8 Figures and Captions

873

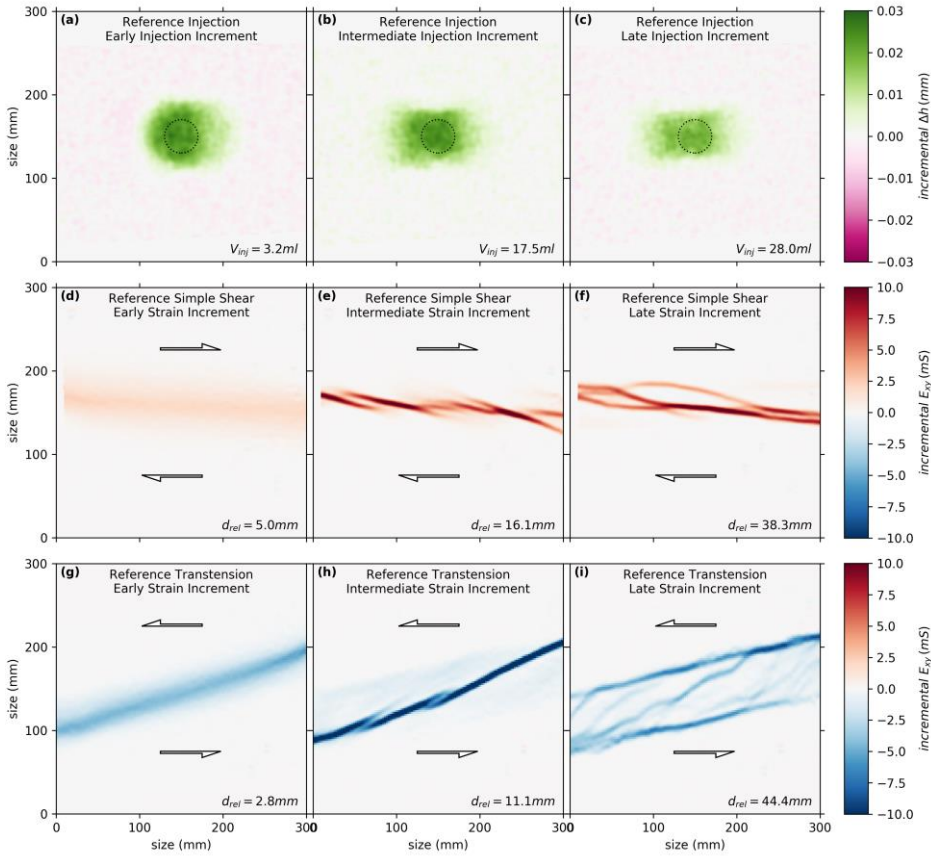


874

875 **Fig. 1** Details of the experimental apparatus. Details of the experimental set-up. (a) Schematic cut-out 3D view
 876 depicting its various components; (b) Model layering; kinematic basal boundary conditions for (c) Sketch of
 877 the experimental setting of the simple shear deformation ($d= 310$ mm) and (d) the transtensional deformation
 878 (obliquity $\alpha=15^\circ$) with the initial (yellow) and final (green) positions of the mobile plates ($w= 40$ mm, $w'= 55.5$
 879 mm, $d= 360$ mm, $d'= 375.5$ mm); Oblique view of experimental settings for (e) simple shear and (f) transtensional
 880 deformation. Arrows indicate the direction of plate movement.

881

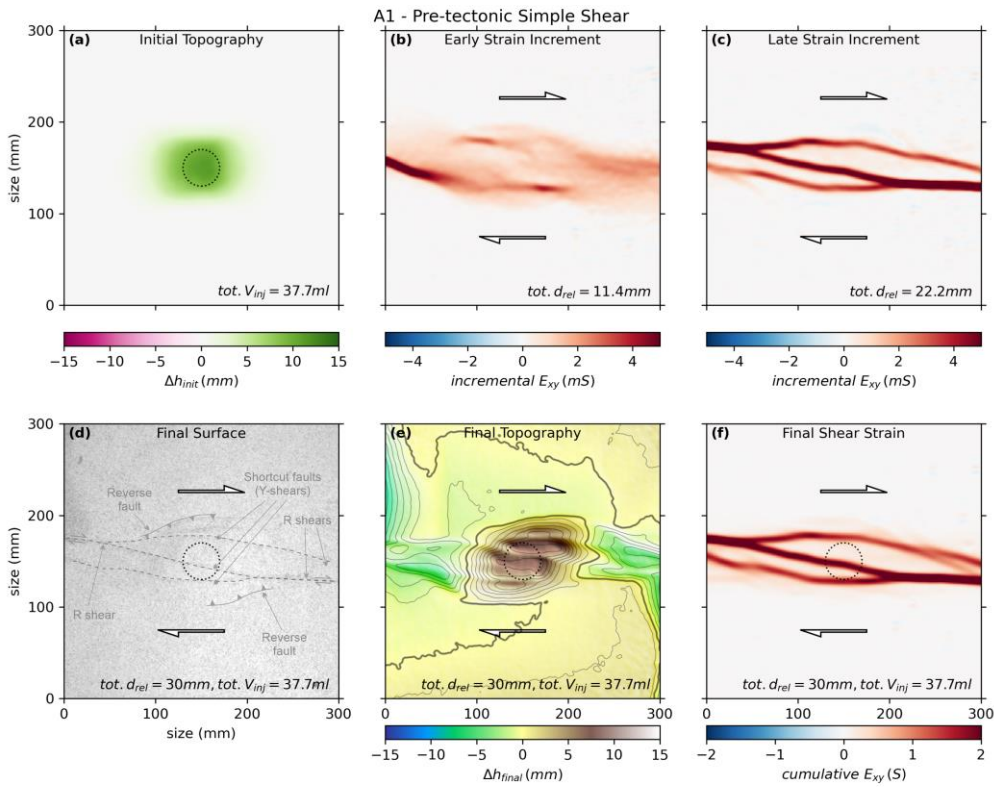
882



883

884 **Fig. 2** Surface evolution and deformational pattern of the reference experiments (Group R): (a-c) representative
 885 stages (with $V_{inj} = 3.2, 17.5, 28.0$ ml) of the topographic evolution (vertical displacement Δh) of the static intru-
 886 sion model R0; (d-f) representative stages (at $d_{rel} = 5.0, 16.1, 38.3$ mm) of the strain field (shear stain E_{xy}) of
 887 the simple shear model RS and (g-i) representative stages (at $d_{rel} = 5.0, 16.1, 38.3$ mm) of the strain field (shear stain
 888 E_{xy}) of the transension model RT. Positive values of E_{xy} (in red) indicate a dextral shear sense and negative
 889 values (in blue) indicate sinistral shear. Dotted circles indicate the position of the basal injection.

890



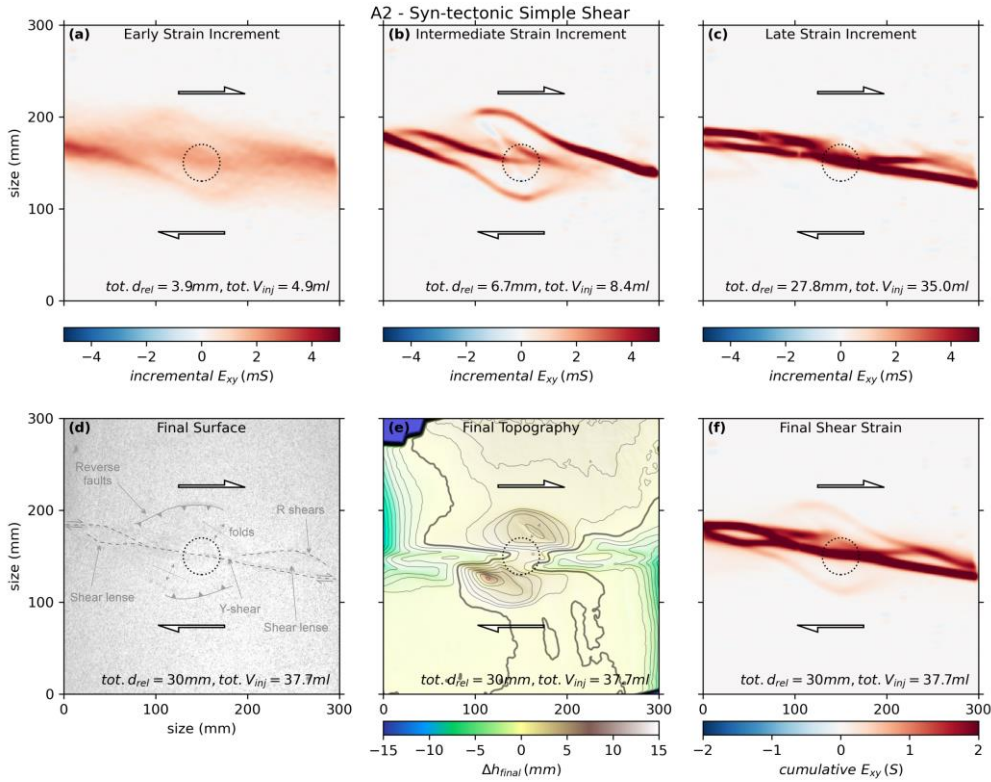
891

892 **Fig. 3** Surface deformation of the pre-tectonic intrusion model in simple shear (Model A1). Shown are snapshots
 893 of the evolution: (a) Topography the end of static intrusion ($V_{inj} = 37.7$ ml), (b) incremental strain during an early
 894 stage of displacement ($d_{rel} = 11.4$ mm), and (c) during a late stage ($d_{rel} = 22.2$ mm). Panels in the second row
 895 show the final (cumulative deformation) stage of the model ($d_{rel} = 30$ mm, $V_{inj} = 37.7$ ml): (d) surface image; (e)
 896 cumulative vertical displacement (tot. $d_{rel}=30mm$) and (f) cumulative shear strain (E_{xy}). Dotted circles indicate
 897 the position of the basal injection.

898

899

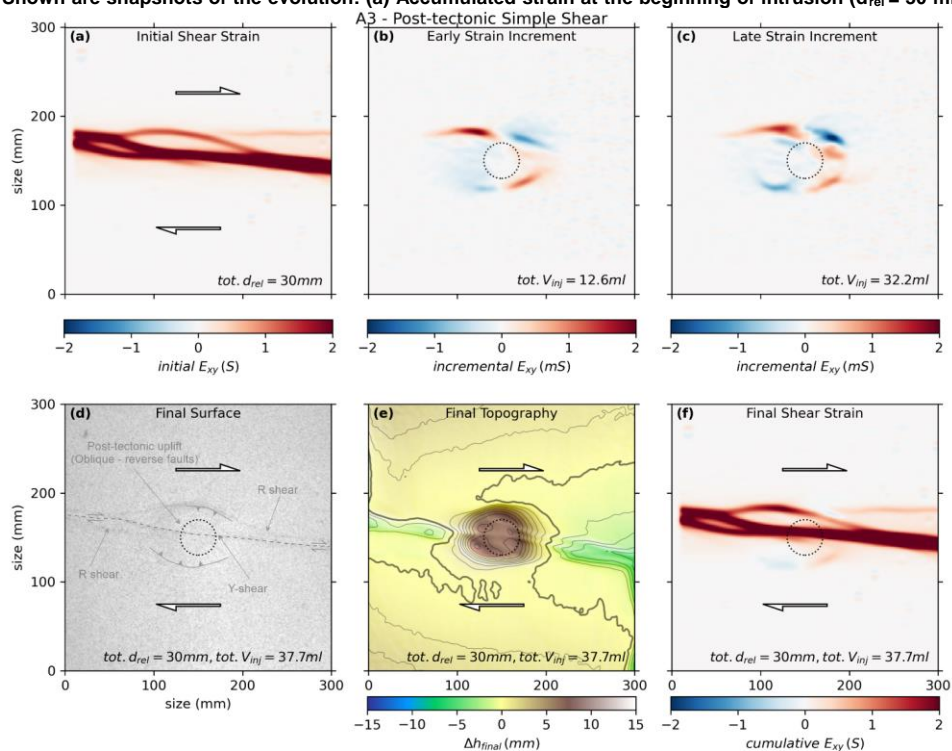
900



901

902 **Fig. 4** Surface deformation of the syn-tectonic intrusion model in simple shear (Model A2). Shown are snapshots
 903 of the evolution: Incremental strain during an (a) early ($V_{inj} = 4.9$ ml and $d_{rel} = 6.7$ mm), (b) intermediate ($V_{inj} = 8.4$
 904 ml and $d_{rel} = 6.7$ mm) and (c) late stage ($V_{inj} = 35.0$ ml and $d_{rel} = 27.8$ mm). Panels in the second row show the
 905 final (cumulative deformation) stage ($d_{rel} = 30$ mm, $V_{inj} = 37.7$ ml): (d) surface image; (e) cumulative vertical
 906 displacement (tot. $d_{rel}=30\text{mm}$) and (f) cumulative shear strain (E_{xy}). Dotted circles indicate the position of the

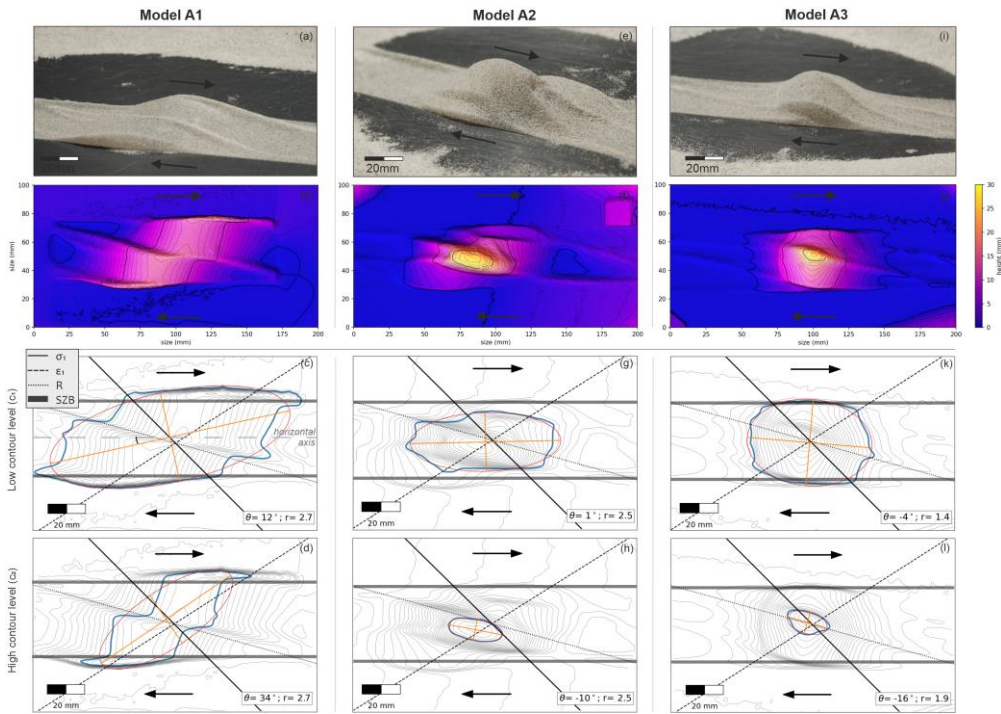
907 basal injection. Fig. 5 Surface deformation of the post-tectonic intrusion model in simple shear (Model A3).
 908 Shown are snapshots of the evolution: (a) Accumulated strain at the beginning of intrusion ($d_{rel} = 30$ mm), (b)



909 incremental strain during an early ($V_{inj} = 12.6$ ml) and (c) late stage ($V_{inj} = 32.2$ ml) of intrusion. Panels in the
 910 second row show the final (cumulative deformation) stage ($d_{rel} = 30$ mm, $V_{inj} = 37.7$ ml): (d) surface image; (e)
 911 cumulative vertical displacement ($tot. d_{rel}=30mm$) and (f) cumulative shear strain (E_{xy}). Dotted circles indicate
 912 the position of the basal injection.

913

914

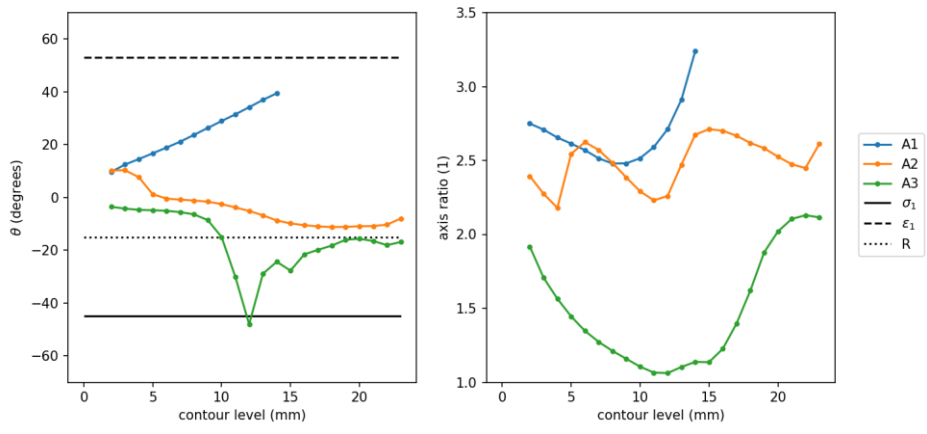


915

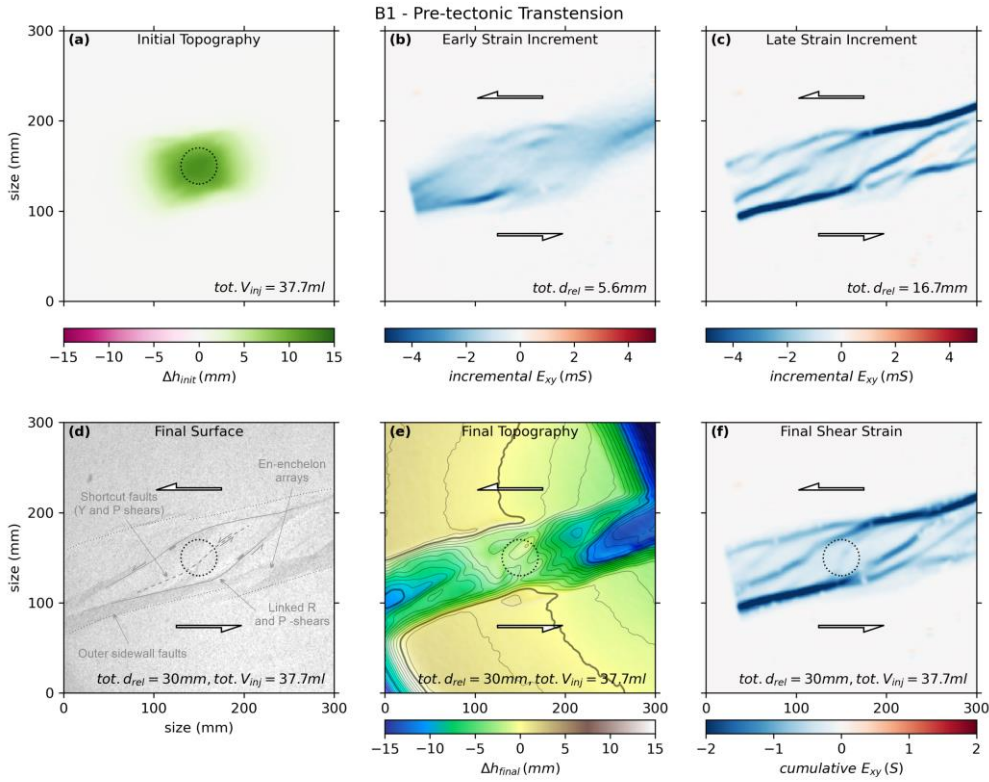
916 **Fig. 6 Models of the intrusions in the simple shear regime (Group A): Model A1 (a-c); Model A2 (d-f) and Model**
 917 **A3 (g-i). (a, d, g) Oblique views of the excavated intrusions; (b, e, h) Digital Intrusion Models (DIM) coloured and**
 918 **with contour lines; (c, f, i) Orientation and geometry of the intrusion (in map view), where θ = the angle between**
 919 **the long axis (orange) of the fitted ellipse (red) and the strike of the basal shear zone. r is the intrusion's aspect**
 920 **ratio (length-to-width ratio, L/W). Light and dark grey quadrants indicate contraction and extensional quadrants,**
 921 **respectively.**

922

923



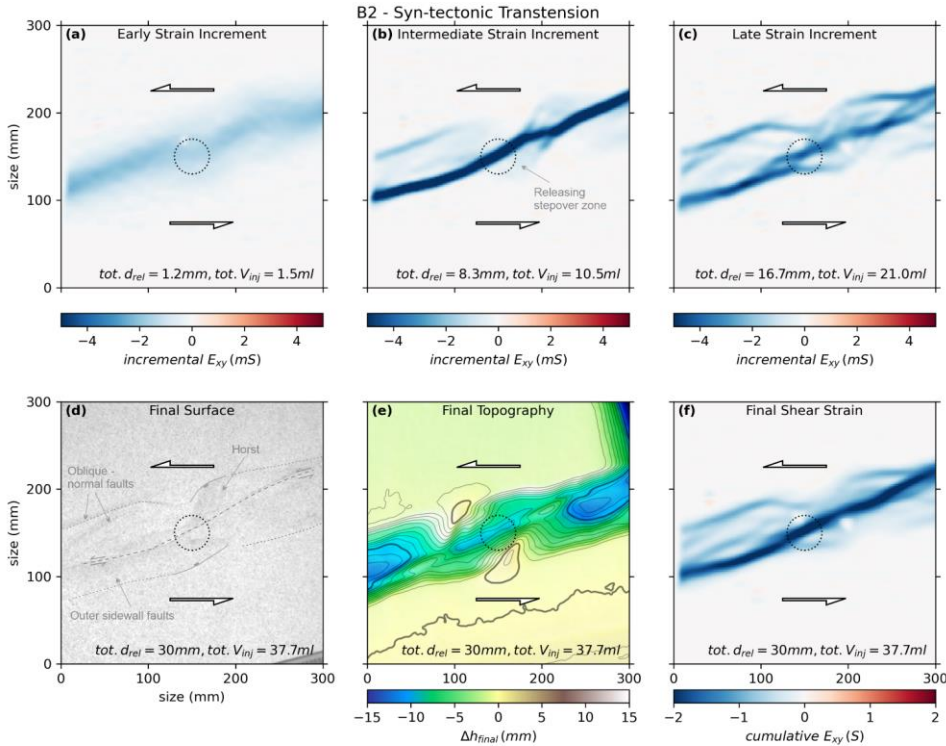
924 Fig. 7 Series A experimental results expressed in graph of angles and ratios ellipses vs. intrusion contour level.



925

926 **Fig. 8** Surface deformation of the pre-tectonic intrusion model in simple shear (Model B1). Shown are snapshots
 927 representative of the evolution: (a) Topography the end of static intrusion ($V_{inj} = 37.7$ ml), (b) incremental strain
 928 during an early stage of displacement ($d_{rel} = 5.6$ mm), and (c) during a late stage ($d_{rel} = 16.7$ mm). Panels in the
 929 second row show the final (cumulative deformation) stage of the model ($d_{rel} = 30$ mm, $V_{inj} = 37.7$ ml): (d) surface
 930 image; (e) cumulative vertical displacement (tot. $d_{rel}=30$ mm) and (f) cumulative shear strain (E_{xy}). Dotted circles
 931 indicate the position of the basal injection.

932



933

934 **Fig. 9** Surface deformation of the syn-tectonic intrusion model in transtension (Model B2). Shown are snapshots
 935 representative of the evolution: Incremental strain during an (a) early ($V_{inj} = 1.5$ ml and $d_{rel} = 1.2$ mm), (b) inter-
 936 mediate ($V_{inj} = 10.5$ ml and $d_{rel} = 8.3$ mm) and (c) late stage ($V_{inj} = 21.0$ ml and $d_{rel} = 16.7$ mm). Panels in the second
 937 row show the final (cumulative deformation) stage ($d_{rel} = 30$ mm, $V_{inj} = 37.7$ ml): (d) surface image; (e) cumulative
 938 vertical displacement (tot. $d_{rel} = 30\text{mm}$) and (f) cumulative shear strain (E_{xy}). Dotted circles indicate the position
 939 of the basal injection.

940

941

942

943

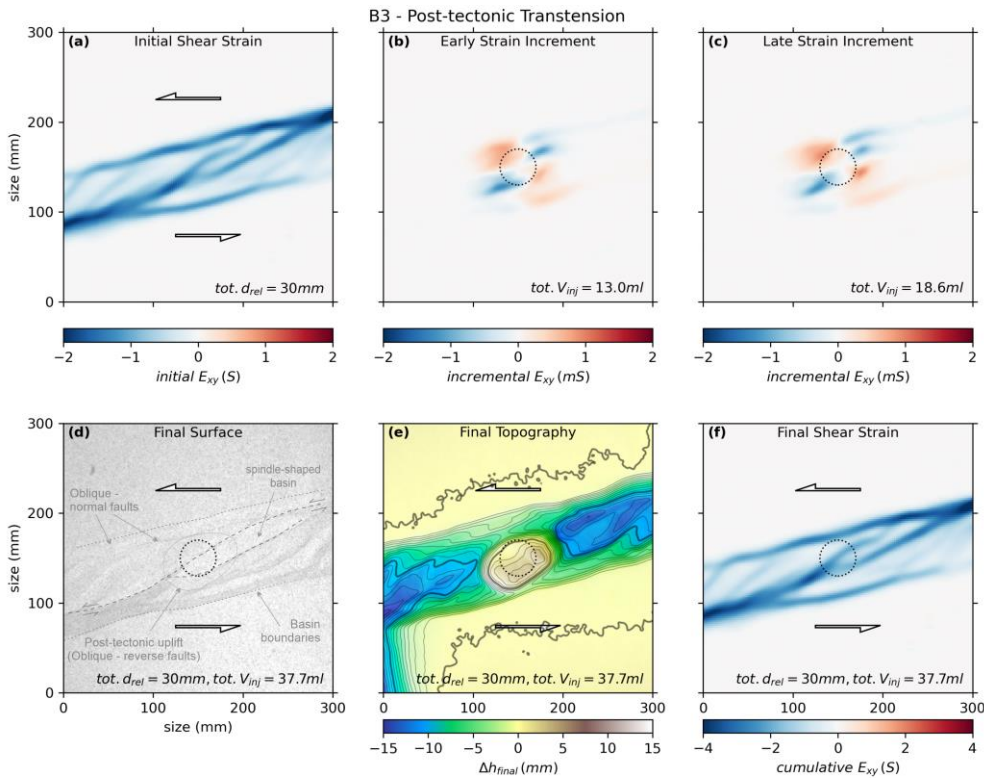
944

945

946

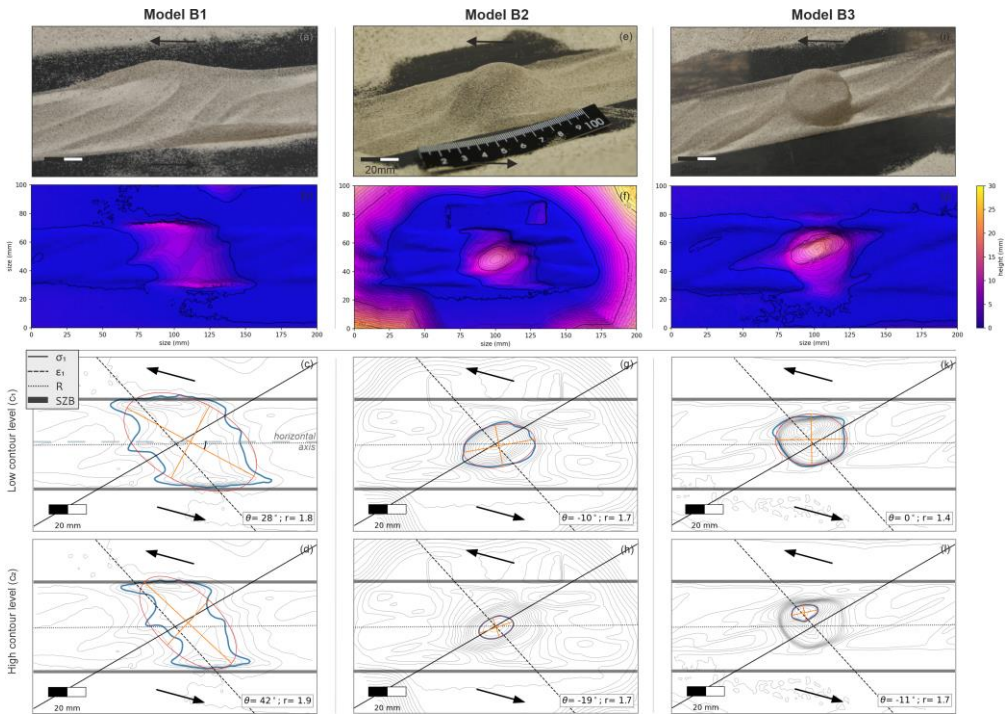
947

948

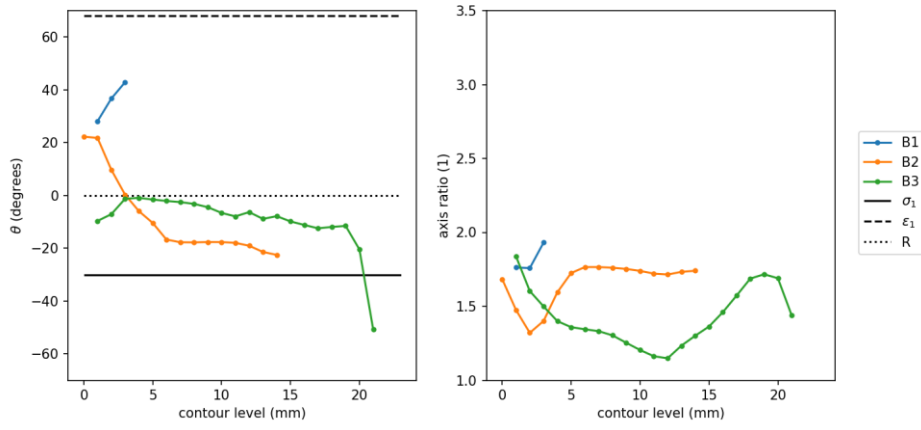


949

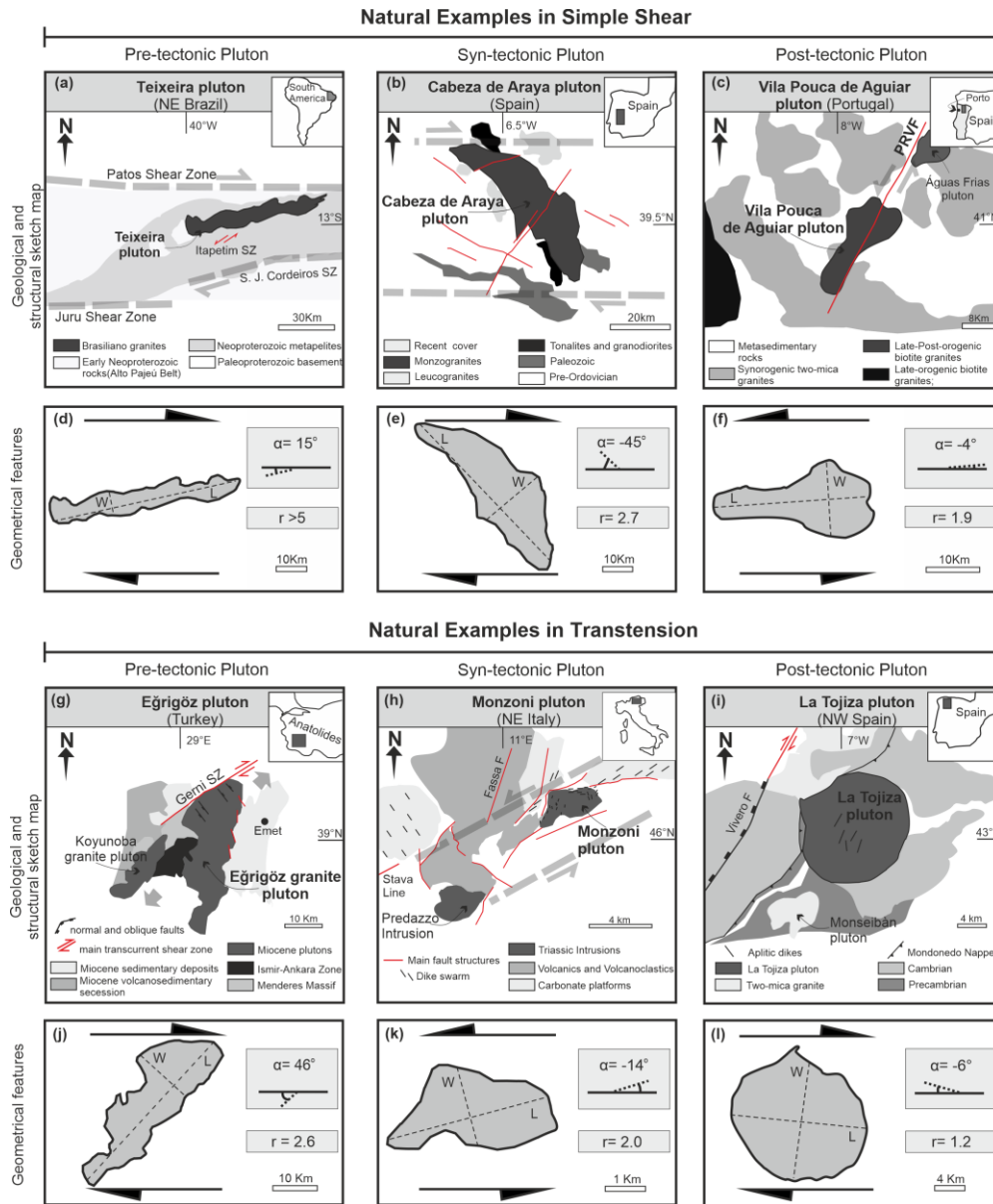
950 **Fig. 10** Surface deformation of the post-tectonic intrusion model in transtension (Model B3). Shown are snapshots representative of the evolution: (a) Accumulated strain at the beginning of intrusion ($d_{rel} = 30$ mm), (b) incremental strain during an early ($V_{inj} = 13$ ml) and (c) late stage ($V_{inj} = 18.6$ ml) of intrusion. Panels in the second row show the final (cumulative deformation) stage ($d_{rel} = 30$ mm, $V_{inj} = 37.7$ ml): (d) surface image; (e) cumulative vertical displacement (tot. $d_{rel}=30$ mm) and (f) cumulative shear strain (E_{xy}). Dotted circles indicate the position of the basal injection.



956
 957 **Fig. 11 Models of the intrusions in the transensional regime (Group B): Model B1 (a-c); Model B2 (d-f) and**
 958 **Model B3 (g-i). (a, d, g) Oblique views of the excavated intrusions; (b, e, h) Digital Intrusion Models (DIM) col-**
 959 **oured and with contour lines; (c, f, i) Orientation and geometry of the intrusion (in map view), where θ = the**
 960 **angle between the long axis (orange) of the fitted ellipse (red) and the strike of the basal shear zone. r is the**
 961 **intrusion's aspect ratio (length-to-width ratio, L/W). Light and dark grey quadrants indicate contraction and**
 962 **extensional quadrants, respectively.**

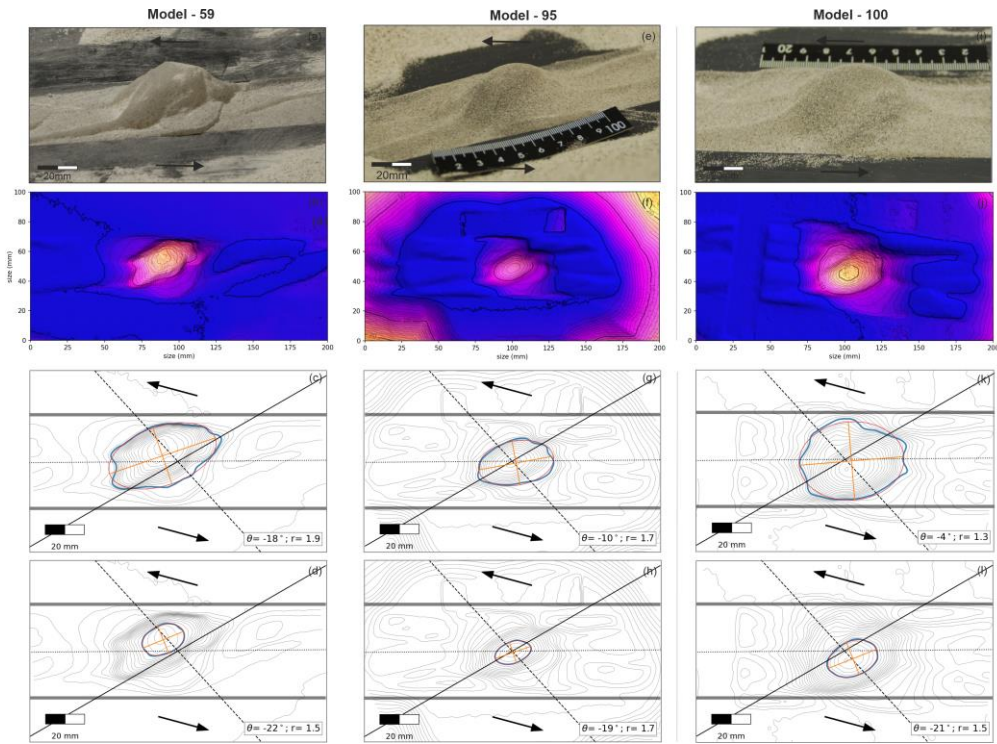


969
970 Fig.12 Series B experimental results expressed in graph of angles and ratios ellipses vs. intrusion contour level.



971
 972 **Fig. 13 Simplified geological maps and shapes of natural plutons emplaced in simple shear and transtensional**
 973 **zones: (a, d) The Teixeira pluton (Archanjo et al., 2008); (b, e) The Cabeza de Araya Pluton (Vigneresse and**
 974 **Bouchez, 1997; Fernandez and Castro, 1999; Corti et al., 2005) and (c, f) The Vila Pouca de Aguiar pluton**
 975 **(Sant’Ovaia et al., 2000). Plutons emplaced in transtensional regime: (g, j) The Eğrigöz pluton is a pre-tectonic**
 976 **intrusion affected by rotation due to the transtensional deformation occurring after the emplacement (Erkül et**
 977 **al., 2017); (h, k) The Monzoni Pluton developed within a transtensional tectonic environment (Sloman, 1989;**
 978 **Bonadiman et al., 1994); (i, l) La Tojiza Pluton is a clear example of post-tectonic intrusion only slightly reactivating**
 979 **the previous transtensional tectonic structures (Aranguren et al., 2003).**

981 9 Appendix



982
 983 Intrinsic variability of intrusion models verified by repeating experiments (Model B2) in syn-tectonic intrusion
 984 in transtension.